Dokumentutgivare
Department of Physics
University of Lund
Handläggare

Dokumentnamn

Dokumentbeteckning

Utgivningsdatum
June 1984

Ärendebeteckning

Författare
J-O Adler
K Hansen
K R Lindgren

LUNFD6/(NFFR-3051)/1-52/(1984)

Dokumenttitel och undertitel

A magnetic electron spectrometer for photonuclear experiments at MAX

Referat (sammandrag)

A magnetic electron spectrometer for tagged photon experiments at the accelerator system MAX has been designed and constructed. A small magnet of the inclined plane pole faces type with opening angle $\pm 8^{0}$ was choosen resulting in a time difference between different electron trajectories of less than 1ns. The focal properties of the spectrometer were investigated by ray-tracings showing that for an angular acceptance of $|\theta_V| \leq 4^{0}$ and $|\theta_H| \leq 8^{0}$ the astigmatic and aberrational effects will contribute less than 10% to the energy resolution of the focal plane detector array.

Referat skrivet av
Authors

Förslag till ytterligare nyckelord

Klassifikationssystem och -klass(er)

Indextermer (ange källa)

Omfång
52 pages

Övriga bibliografiska uppgifter

Språk
English

Sekretessuppgifter

ISSN

ISBN

Dokumentet kan erhållas från
Department of Physics
University of Lund
Sölvegatan 14, S-223 62 Lund, Sweden

Pris

Mottagarens uppgifter

A MAGNETIC ELECTRON SPECTROMETER FOR PHOTONUCLEAR EXPERIMENTS AT MAX

J-O Adler, K Hansen and K R Lindgren

Department of Physics, University of Lund, Sölvegatan 14,

S-223 62 Lund, Sweden

A magnetic electron spectrometer for tagged photon experiments at the accelerator system MAX in Lund has been designed and constructed. A small magnet of the inclined plane pole faces type with opening angle $\pm 8^{o}$ was choosen resulting in a time difference between different electron trajectories of less than 1ns. The focal properties of the spectrometer were investigated by ray-tracings in the measured field showing that for an angular acceptance of $|\Theta_V| \leq 4^{o}$ and $|\Theta_H| \leq 8^{o}$ the astigmatic and aberrational effects will contribute less than 10% to the energy resolution of the focal plane detector array.

1 INTRODUCTION

The future in nuclear physics research with electromagnetic probes lies highly in the development of electron accelerator systems with high duty factor. Such a system is presently being built in Lund. The system, called MAX, consists of a 100 MeV racetrack microtron connected to a pulse stretcher ring. The system is described in[1)].

With continuous electron beams new areas of coincidence experiments are opened in nuclear physics. The most competitive experiments that will be possible at MAX are experiments with monoenergetic photons. Due to the high duty factor the so called photon tagging technique can be used. This technique, which is illustrated in fig. 1, gives at present the best resolved monoenergetic photon source with continuously variable energy.

Electrons with energy E_0 are allowed to hit a thin radiator giving rise to a continuous bremsstrahlung spectrum with maximum energy E_0. If the radiator is thin and E_0 high enough ($\geq$ 10 MeV) the interacting electron will give rise to a γ-quantum with energy

$$E_\gamma = E_0 - E_r$$

where E_r is the energy of the scattered electron that emerges from the radiator. Most of the electrons will, however, pass through the radiator without interaction. The post-bremsstrahlung electrons are energy analyzed in a magnetic spectrometer. The bremsstrahlung photons proceed to a reaction target where different types of nuclear reactions may take place. The reaction product (p, n, α, γ etc) of interest in the actual experiment is detected and coincidences between pulses from the product and electron detectors determine the photon energy. The photon energy resolution, ΔE_γ, is mainly determined by the resolution of the magnetic spectrometer and the width of the focal plane detectors. By using a broad range spectrometer and many detectors in the focal plane a large part of the photon spectrum can be covered in a single run.

In this paper we describe the magnetic spectrometer, which has been constructed for this type of experiments in Lund. Theoretical calculations for the construction, field measurements and ray tracing to determine the focal plane properties are described. This paper will be followed by further papers concerning the detector equipment and the behavior of the spectrometer in actual experiments.

2 TYPE OF SPECTROMETER

When choosing type of electron spectrometer the need for large solid angle and broad energy range has been decisive. Fig. 2 shows the calculated angular distribution of electrons from a thin radiator after radiating a γ-quantum in the giant resonance region (E_0 = 25 MeV, E_γ = 22 MeV). The distribution has been calculated with a Monte Carlo program[2]. Maximum photon angle in the calculation was 0.04 rad. As shown in the figure the angular distribution becomes broad and high detection efficiency for post-bremsstrahlung electrons in this energy range means a spectrometer with large solid angle. This can be achieved in a simple way by using a magnet with inclined plane pole faces. This type of spectrometer, which combines large solid angle with double focusing, was first described by Richardson[3] and has later on been used for tagging experiment at the University of Illinois[4,5].

Our spectrometer has an effective opening angle of $\pm 8^\circ$ (determined by the vacuum chamber) corresponding to a solid angle of 0.03 sr and, as will be shown later, a momentum bite of 40% of the mean focal plane momentum.

The number of electrons entering the spectrometer after having radiated a photon depends on the ratio E_γ/E_0. The larger this value the smaller the spectrometer capture efficiency P_{tagg}. However, for a given value of E_γ/E_o the efficiency increases with E_o as both bremsstrahlung and electrons are emitted at smaller angles. Fig. 3 shows P_{tagg} as a function of E_o for two different values of E_γ/E_o.

3 THE IDEAL MAGNET

For an ideal magnet with inclined plane pole faces the field inside the gap is given by

$$B \sim 1/r$$

where r is the distance to the intersection line between the pole faces. Outside the magnet the field is zero. In fig. 4 the magnet has been positioned in a coordinate system and certain angles and distances defined. For the magnet in question h = 21 mm.

Calculation of electron orbits in such an ideal magnet has been made by O'Connell[4]. Solution of the equations of motion results in a first order focus given by

$$Z = 2Z_o(K^2 I(K,\pi/2)-1)$$

$$X = 2Z_o K I(K,\pi/2)$$

where K is a momentum-dependent constant and $I(K,\pi/2)$ is given by

$$I = \int_{\pi/2}^{0} \cos(\theta) e^{K\cos\theta}\, d\theta$$

The angle θ is defined as the angle between the tangent to the particle orbit and the X-axis and Z_o is the distance between the X-axis and the front pole edge. By varying K for Z_o = 113 mm the position of the focal points in the horizontal plane has been calculated. Their location is given by the dot-dashed curve in fig. 5. In the horizontal plane the spread in the focal width (ΔX = astigmatic width) is given by the opening angle $\pm\,\theta_H$ between the rays from a point source. For the ideal magnet the relative width is given by

$$\Delta X/X = 1/2\{K^2 - (I(K,\pi/2))^{-1}\}(\theta_H)^2$$

with the same notations as above. The horizontal focal width is thus a quadratic function of the horizontal angular divergence θ_H.

With $\theta_H = \pm\,8^0$ and appropriate values for K and I the horizontal focal width ΔX was calculated along the focal plane (1). The result is shown in the lower part of fig. 6. As shown in the figure we get a minimum (ΔX=0) at the intersection line between the pole faces.

4 THE REAL MAGNET

4.1 Calculations of magnetic field and ray-tracing

In order to dimension and investigate the focusing properties of a real magnet with fringe fields a two-dimensional magnetic field map was calculated with the computer program MAGNET[6)]. With this program the field in the iron and air can be determined. The iron air profile (Y-Z plane in fig. 4) was divided into a quadratic network. In the nodes of this network the field was calculated. The field distribution obtained is given in fig. 7. Due to the limited computer memory capacity the length of the sides of the squares could not be chosen to be less than 5 mm, which gave an insufficient accuracy in the ray-tracing. Hence a division of the field in the direction of the Z-axis was done as follows. In the region of about ± 3h around the front pole edge, where the greatest field variations appear, the field calculated with a square size of 5x5 mm was transformed into a square size of 1x1 mm with the aid of a spline function. Further inside the magnet the field was assumed to follow the theoretically expected $B = B_0/r$ dependence (r defined according to fig. 4a). The constant B_0 was determined to get overlap with the field in the neighbouring regions. The field values obtained from this function deviated less than 1% from those calculated with the computer program MAGNET. Outside the front edge of the magnet (>3h) a polynomial of sixth order was fitted to the fringe field calculated with MAGNET. This fit included a region 300 mm away from the front edge. For all calculated points the deviation from the fitted curve was less than 0.5%. Outside this region a linear fit could be used.

To get an estimate of the horisontal focusing properties of the magnet, ray-tracing in the field distribution described above was carried out. A computer program to calculate electron orbits from the bremsstrahlung target position to the focal plane was written. The field components along the coordinate axes **were** determined and changes in the electron trajectories were calculated in small steps. In the calculations the primary electron beam was supposed to hit the radiator perpendicular. The radiator was placed on the line of intersection of the extended polefaces i.e. 113 mm from the front pole edge, in the point X = 10 mm, Y = Z = 0. The secondary electrons were emitted with an angle $\theta_H = 0^o$ and $\pm 8^o$ with respect to the primary beam direction (see fig. 4b). Calculations were first done for a magnet with a depth of 50 cm and a width of 100 cm. However, with such a large magnet the path difference between the shortest and longest trajectory for electrons of the same energy was too large, which ment that the desired time resolution could not be achieved. The magnet size was therefor reduced by a factor of two, which led to a time difference at focus of less than 1 ns for electrons emitted in $+ 8^o$ and $- 8^o$. The position of the horizontal focus calculated with the theoretical field is given by the dashed curve in fig. 8. A comparison with the result for the ideal magnet (see also fig. 5) shows that the focal plane is moved out from the front edge, which is an effect of the fringe field. The change in position is between 4 and 10 cm. This is advantegous since focus for the low energy electrons now appear outside the pole gap of the magnet. In a second approach the primary electron beam was supposed to enter the radiator with an angle less than 90^o. However, no improvements of the focusing properties compared to perpendicular entrance could be achieved.

4.2 Measurements of magnetic field and ray-tracing

After the magnet had been manufactured (see section 4.3) the field was measured in the median plane inside and outside the pole gap with the aid of a calibrated Hall-probe. A detailed description of calibration and measurement procedures are given in Appendix A. The field distribution at a current of 40A is shown in fig. 7. In this figure the values obtained with the program MAGNET are also given. Normalization to the measured values was done at the peak field. A very good agreement between the two distributions is obtained, except in the back pole-gap, where the true field is smaller due to field leakage. Also for the front fringe field the calculated and measured values differ somewhat.

One would expect the form of the field distribution to be independent of the current through the coils. By calculating the difference between the field measured for different currents it could be checked that no systematic errors affect the measurements. Such a check is shown in fig. 10, where the difference (ΔB) between the fields measured at 40 and 150 A after normalization at the peak fields has been plotted. As seen in the figure the points scatter randomly about zero and the deviation is always less than $\pm$ 3 Gauss.

With the length of the magnet (along the X-axis) the field should not vary. Close to the coils, however, one could expect some deviation. In order to check this the peak field (9mm into the magnet measured from the front edge) was measured for different X coordinates. The results are shown in fig. 11. Within the range which will be used the relative deviations from the mid-magnet values are always less than 4 o/oo.

Using the measured fields new ray-tracing were carried out. In fig.5 the horizontal focus obtained from the field measured at a current of 40A is shown. The outermost orbit (E_r = 4.6 MeV) which will be possible to detect will pass 16 cm into the magnet, i.e. always in the 1/r dependent field. The innermost orbit which will be detected corresponds to E_r = 3.0 MeV. This means that the energy range of the spectrometer will be about 40% of the average electron energy.

In order to investigate the homogeneity of the field measurements, ray-tracings with the fields obtained at three different currents were also done. As seen in fig. 8 the position of the focal plane is independent of the absolute magnitude of the field. In this figure is also shown the change in focal plane position when the tracing is done with measured and calculated fields respectively. The observed displacement is explained by the fact that the true fringe field is larger than the calculated one (see fig.7).

Ray-tracings were also done with the field shielded,i.e. B_{fringe} suppressed to simulate a magnetic shield, outside the front edge of the magnet. The focus obtained is shown in fig. 9. The difference observed compared with fig. 8 is that the focal points for small orbits are moved somewhat closer to the front edge, which means that the focal plane make a somewhat larger angle with respect to this edge.

From the ray-tracings the image width ΔX is obtained. This quantity is defined as the minimum distance between the electron trajectories for 0^o and $\pm\ \theta_H$. The width along the focal plane (astigmatic broadening) calculated with the true field is given in the upper part of fig. 6. As seen in this figure, no $\Delta X = 0$ is obtained, but the width displays a weak minimum for small orbits. It should also be observed that the width in this case is overall smaller compared to the result for the ideal magnet. As is clear from the formula for the ideal magnet one should theoretically expect the image width in the horizontal plane to increase as the square of the initial opening angle between the electron orbits. Calculations shows that this is also the case for the true magnetic field. This is shown in fig. 12 where ΔX is plotted as a function of half the opening angle. The results for three different electron energies are given.

We have also investigated how the horizontal resolution depends on the distance between the bremsstrahlung target and the front pole edge (Z_t). Ray-tracing in the measured field was done for four different opening angles (θ_H) and the results are given in fig. 13. For all angles a strong minimum is obtained when the radiator is placed about 50 mm from the pole edge. These results can be compared with similar investigations by Knowles et al[5] showing great resemblances. The position of the focal plane is of course determined by the position of the radiator with respect to the front pole edge. The horizontal focus is parallelly moved in the Z-direction as much as the radiator is moved in the same direction, see fig. 14.

Finally we have studied the aberrational broadening of the focal point by ray-tracings out of the horizontal plane, $\theta_V \neq 0$. To be able to do this the magnetic field outside the median plane was calculated using a Taylors expansion. In the coordinate system shown in fig. 4 the different field components may be written[7]

$$B_X(Y,Z) = 0$$

$$B_Y(Y,Z) = B_1 - B_3 + \dots$$

$$B_Z(Y,Z) = B_0 - B_2 + \dots$$

where

$$B_n = \frac{1}{n!} B^{(n)}(Z) Y^n$$

$$B^{(n)} = \frac{d^n B_Y(0,Z)}{dZ^n}$$

These series converge rapidly and only terms B_n with $n \leq 3$ need to be included. The derivatives $B^{(n)}$ have to be calculated numerically from the measured $B_Y(0,Z)$ see Appendix B.

The result of the ray-tracing is shown in fig. 15 for electrons with E_r = 8 MeV and for four different horizontal opening angles i.e. $\theta_H = \pm 2^\circ$, $\pm 4^\circ$, $\pm 6^\circ$ and $\pm 8^\circ$. Four different vertical angles θ_V were used. The figure shows the X, Y-coordinates of the electrons at Z = 46 mm corresponding to the focus in the median plane. As can be seen the horizontal opening angle now causes both a horizontal and a vertical defocusing of the beam.

Ray-tracings were extended to two more energies E_r and in fig. 16 the focal widths, i.e. the horizontal widths, caused by the astigmatic broadening and vertical defocusing, have been plotted as horizontal lines at the proper $\langle Y \rangle$-value. The plot has been made in the horizontal focal plane for four different angles θ_V. For each setting (θ_V, E_r) the focal widths for the four different horizontal opening angles (see above) are shown. (For $\theta_V = 0$ the overall width for $|\theta_H| \leq 8^o$ is shown.)

Both figure 15 and 16 show that together with this width there is also a horizontal displacement of the focal points which contribute to the overall horizontal width, i.e. to the energy resolution. Table 1 shows this overall focal width at three different parts of the focal plane and for different limitations on θ_V and θ_H. As can be seen the focal width is most sensitive to restrictions on θ_V.

TABLE 1

$\lvert\theta_V\rvert$ (degrees)	$\lvert\theta_H\rvert$ (degrees)	Overall focal width (mm) at low energy	centre	high energy
$\leq$ 6	$\leq$ 8	9.0	5.4	3.2
$\leq$ 6	$\leq$ 6	7.7	4.4	2.6
$\leq$ 4	$\leq$ 8	4.3	2.9	2.8

The focal plane detector array will consist of plastic scintillators with a width in the X-direction of $\Delta X_{det} = 10$ mm. This means that for an angular acceptance of $|\theta_V| \leq 6^o$ and $|\theta_H| \leq 8^o$ the astigmatic and aberrational effects will contribute about 35% to the energy resolution at the low energy end of the focal plane and about 5% at the high energy end. For $|\theta_V| \leq 4^o$ and $|\theta_H| \leq 8^o$ the corresponding figures are 9% and 4% respectively.

For the ideal magnet, with $B \sim 1/r$ inside the magnet and no fringe field, the vertical focus lies in the plane $Z = 0$ (see Fig. 4). At the intersection between this plane and the focal plane the ideal magnet thus should be double focusing. This corresponds to

E_r = 9 MeV in fig. 16 and as can be seen the real magnet has no vertical focus at this point. This is due to the fringe field and the field the first few centimeters inside the pole gap in the real magnet, which are not proportional to 1/r (see fig. 7) and thus have a component which deflects the beam out of the plane of motion (θ_V = const.). The influence on the vertical focusing depends on θ_V and becomes relatively less important for larger values on θ_V which can be seen in fig. 17. This is the reason for the shift in order between the focal lines for different θ_V-values along the focal plane seen in fig. 16.

4.3 Mechanical design

A schematic drawing of the magnet is shown in fig. 18. All parts of the magnet were manufactured from carbon-iron and the dimensions were determined from the earlier described calculations with the program MAGNET (e.g. the thickness of the iron) and ray-tracings. Between the coils there is an area (25x60 cm) where a vacuum chamber will be placed. The height of the pole-gap opening in the front edge is 2h = 4.2 cm and half the opening angle is 10.4^o (see also fig. 4). Due to the vacuum chamber this angle will be reduced to effectively 8^o.

The two coils consist of copper wire, each wired 125 turns. The wire has a square cross section (6.6x6.6 mm) and is hollow (Ø = 4 mm) to make water cooling possible. The effective cross section is 31 mm^2. The two coils are coupled in series and constitute a total resistans of about 0.2 ohms. To achieve effective water cooling each coil was divided into five subcoils, which are supplied with water in parallell.

The maximum magnetic field (9mm inside the magnet measured from the front edge) which can be obtained is 6.5 kGauss. This is achieved at a current of 300 A. With this field it is possible to analyse electrons with a kinetic energy of 24 MeV. However, already at 4.5 kGauss the iron starts to be saturated (see fig. 19). At this field up to 15 MeV electrons can be analysed, which is sufficient for most applications.

ACKNOWLEDGEMENTS

The authors wish to acknowledge the support of the Gambro cooperation for letting one of us (K. Hansen) hold their Gambro gamma scholarship while participating in this projekt. We also would like to thank Professor Mikael Eriksson for his help with the basic magnet calculations and general interest in the work.

References:

1) M. Eriksson, Nucl. Instr. Meth. 196 (1982)331

2) J-O. Adler, priv. com.

3) H.O.W. Richardson, Proc. Phys. Soc. 59 (1947)791

4) J.S. O'connell, Rev. Sci. Instr. 32 (1961)1314

5) J.W. Knowles et al., Nucl. Instr. Meth. 193 (1982)463

6) "MAGNET"-program, CERN program library T600, C. Iselin

7) K.L. Brown, Adv. Part. Phys. Intersc. 1 (1967)71

FIGURE CAPTIONS

Fig. 1 Schematic representation of the tagged-bremsstrahlung technique.

Fig. 2 Calculated angular distributon of electrons from a thin radiator, after radiating a 22 MeV γ-quantum. The incident electron energy is 25 MeV and the maximum photon angle 0.04 rad.

Fig. 3 The capture efficiency, P_{tagg}, for the spectrometer (effective opening angle $\pm 8^{o}$) as a function of E_{o} for different maximum photon angles. The solid curve shows the result for $E_{\gamma}/E_{o} = 0.88$ and the dot-dashed curve the result for $E_{\gamma}/E_{o} = 0.63$.

Fig. 4 The spectrometer magnet a) in the (Y,Z) plane and b) in the (X,Z) plane. Certain distances and angles are defined.

Fig. 5 Result of ray-tracings in the measured field. The kinetic energy of the electrons are shown together with the position of the focal plane. The opening angle used is $\theta_{H} = \pm 8^{o}$.The dot-dashed curve shows the position of the focal plane for the ideal magnet. The direction of the main beam (dashed curve) and its divergence for an opening angle of $\pm 1^{o}$ is also shown for two different values of $\eta(=E_{\gamma}/E_{o})$.

Fig. 6 Focal width in the horizontal, (X,Z)-,plane along the focal plane (1) for the ideal magnet (lower part) and in the measured field (upper part).

Fig. 7 A comparison between the magnetic field along the Z-axis calculated with the program MAGNET and measured at a current of 40A in the coils. The values are normalized at the peak field.

Fig. 8 Horizontal focus calculated from measured field values for three different currents in the coils. The dashed curve is obtained from the theoretically calculated field. Opening angle between the orbits was $\theta_{H} = \pm 2^{o}$.

Fig. 9 Same as fig.8 but with suppressed field outside the front edge.

Fig. 10 Field difference (ΔB) along the Z-axis between fields measured at 40 and 150 A currents. The differences were calculated after normalization of the 40 A peak field to that for 150 A.

Fig. 11 The relative variation of the peak field in the horizontal plane determined from measurements along the X-axis. The measurements starts in the middle of the magnet. The resolution in the measurements is 1 gauss corresponding to 0.9 o/oo.

Fig. 12 The square-root of the horizontal image width as a function of the opening angle (θ_H) between the electron orbits. In the calculations measured fields were used and values for three different electron energies are given.

Fig. 13 Horizontal resolution as a function of the distance (Z_t) between bremsstrahlung target and the front pole-edge. Calculations are made with four different values of θ_H.

Fig. 14 Position of the horizontal focus for five different distances (50, 70, 90, 110 and 130 mm) between radiator and front pole-edge.

Fig. 15 Result of ray-tracings out of the horizontal plane. The X, Y-coordinates for rays with given values on θ_V and θ_H ($+\theta_H$ or $-\theta_H$) are plotted at the Z-value given, which corresponds to the focus in the median plane for electrons with E_r = 8 MeV (low energy end of the focal plane, see also fig. 16).

Fig. 16 Result of ray-tracings out of the horizontal plane. The focal width for rays with a given θ_V-value and within a certain horizontal opening angle θ_H is plotted as a horizontal line at the mean Y-value, $\langle Y \rangle$, for a range of θ_V- and θ_H-values and for three different energies E_r. All the data are given in the focal plane (the corresponding Z-coordinates are given at the top of the figure). The length of the horizontal lines give the focal width for each setting and the number adjacent to each line the θ_H-value in degrees. For $\theta_V = 0$ the overall width for $|\theta_H| \leq 8^o$ is shown.

Fig. 17 Electron orbits in the spectrometer projected on the (Y,Z)-plane. At the choosen energy, $E_r = 9$ MeV, the focal plane falls at Z = 0.

Fig. 18 A schematic drawing showing the mechanical design of the magnet.

Fig. 19 The peak field as a function of the current in the coils. The solid curve is the result of measurements and the dashed curve shows the ideal case with no saturation.

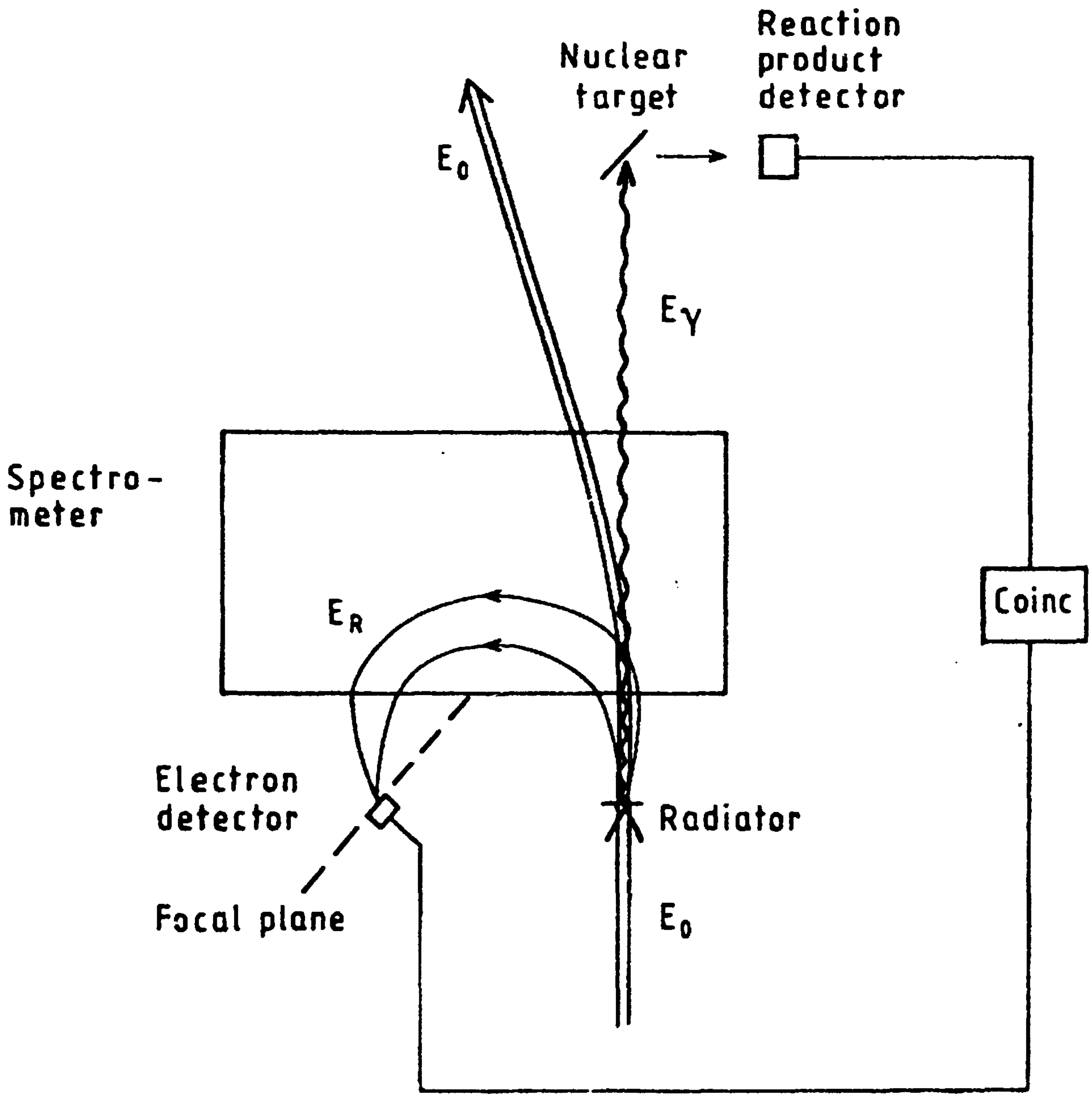
Reaction
product
detector
Nuclear
target
E0
Eγ
Spectro-
meter
Coinc
ER
Electron
detector
Radiator
Focal plane
E0

FIG. 1

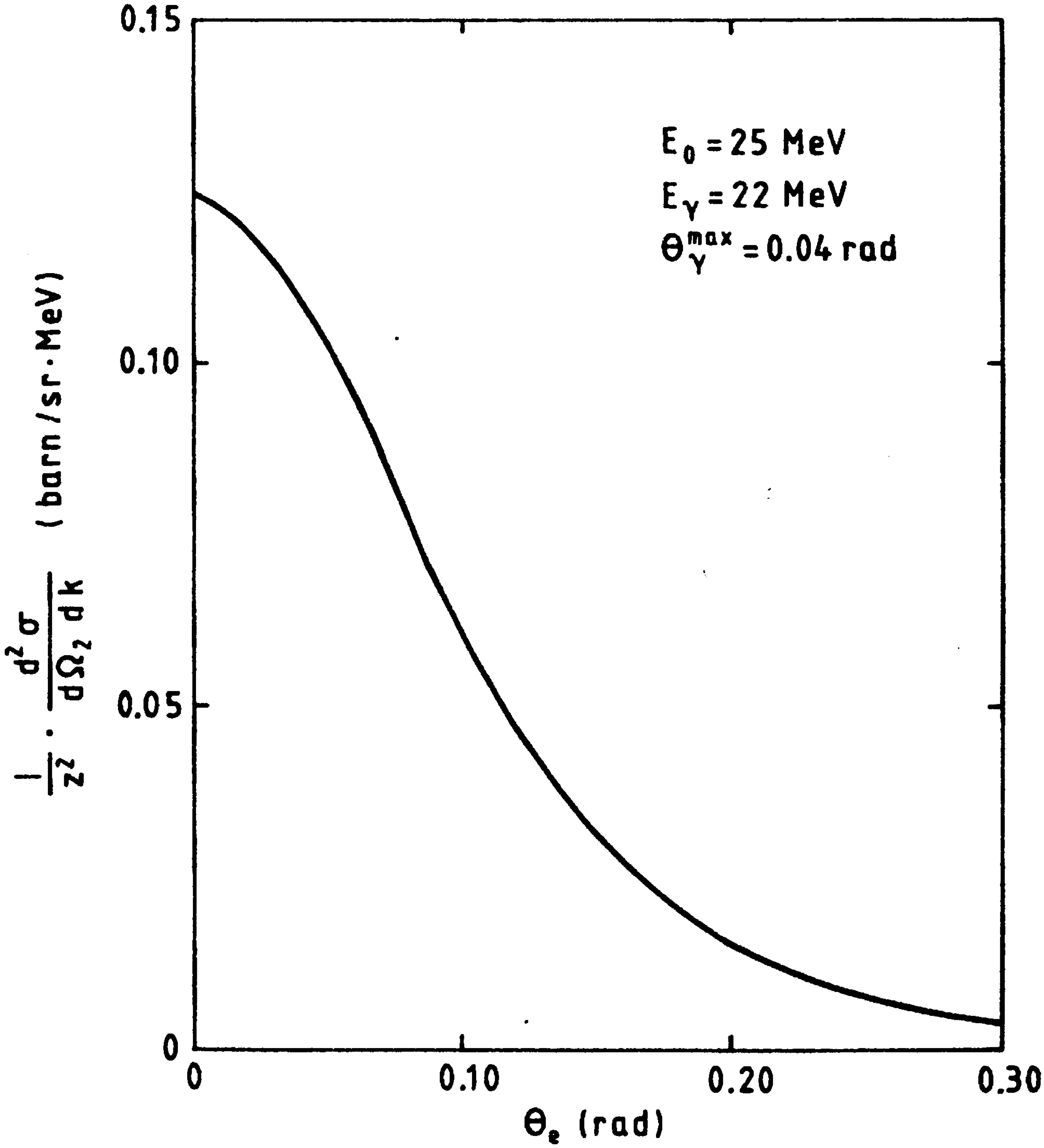

$E_0 = 25$ MeV
$E_\gamma = 22$ MeV
$\Theta_\gamma^{max} = 0.04$ rad
$\frac{1}{Z^2} \cdot \frac{d^2\sigma}{d\Omega_2\, dk}$ (barn/sr·MeV)
0.15
0.10
0.05
0
0
0.10
0.20
0.30
Θ_e (rad)

FIG. 2

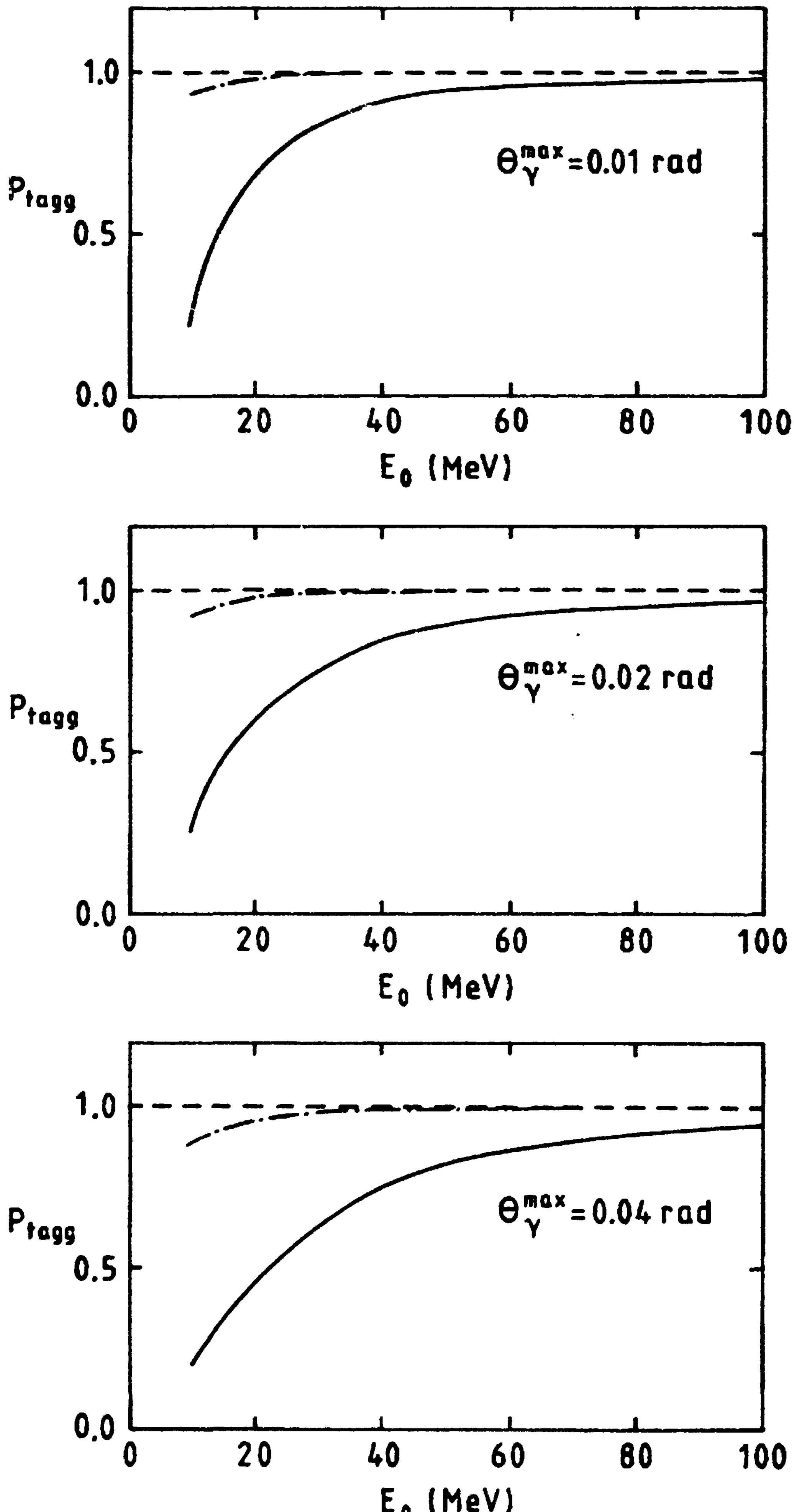

1.0
0.5
0.0
P_{tagg}
Θ_γ^{max}=0.01 rad
0
20
40
60
80
100
E_0 (MeV)
Θ_γ^{max}=0.02 rad
Θ_γ^{max}=0.04 rad

FIG. 3

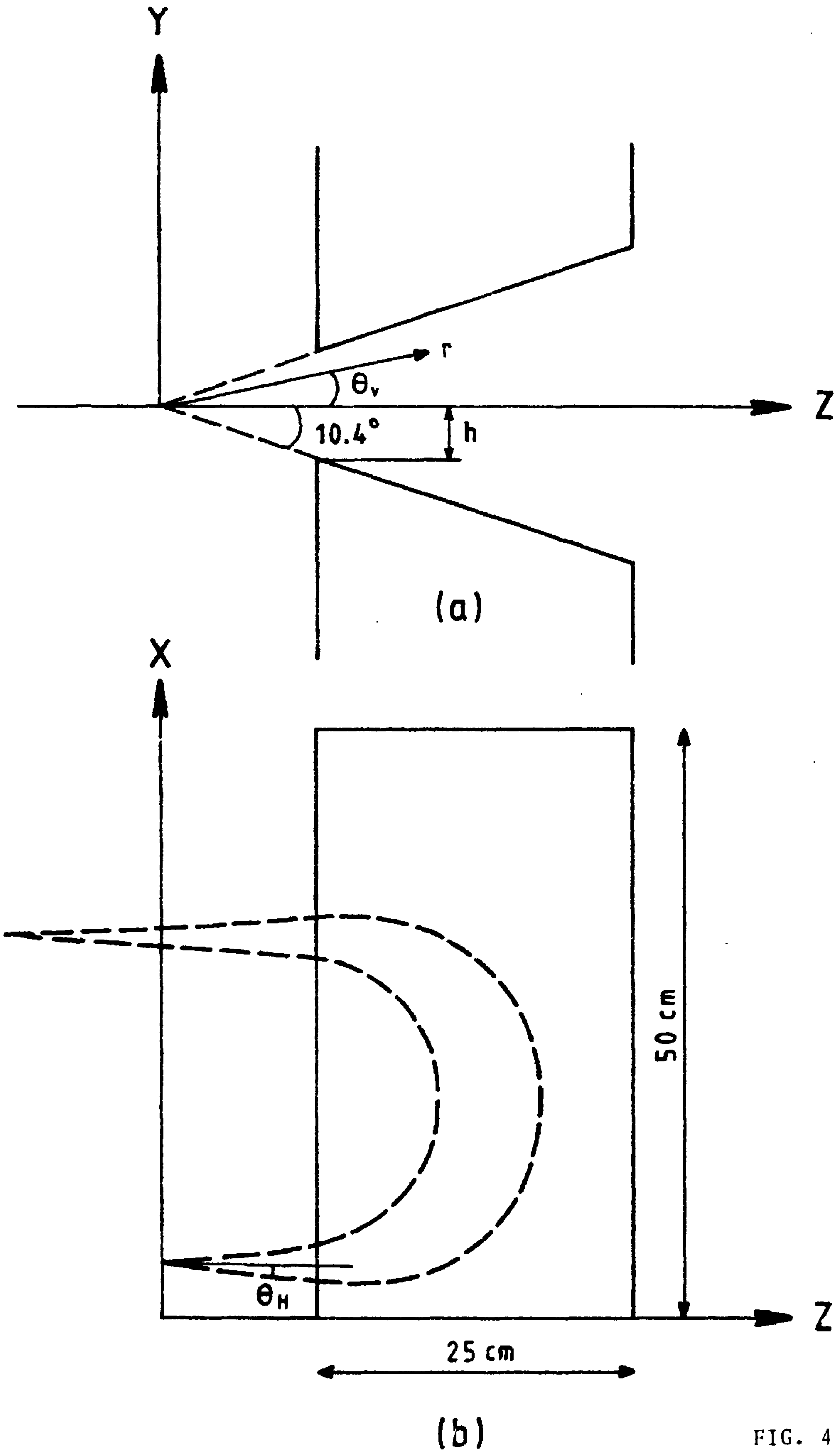

FIG. 4

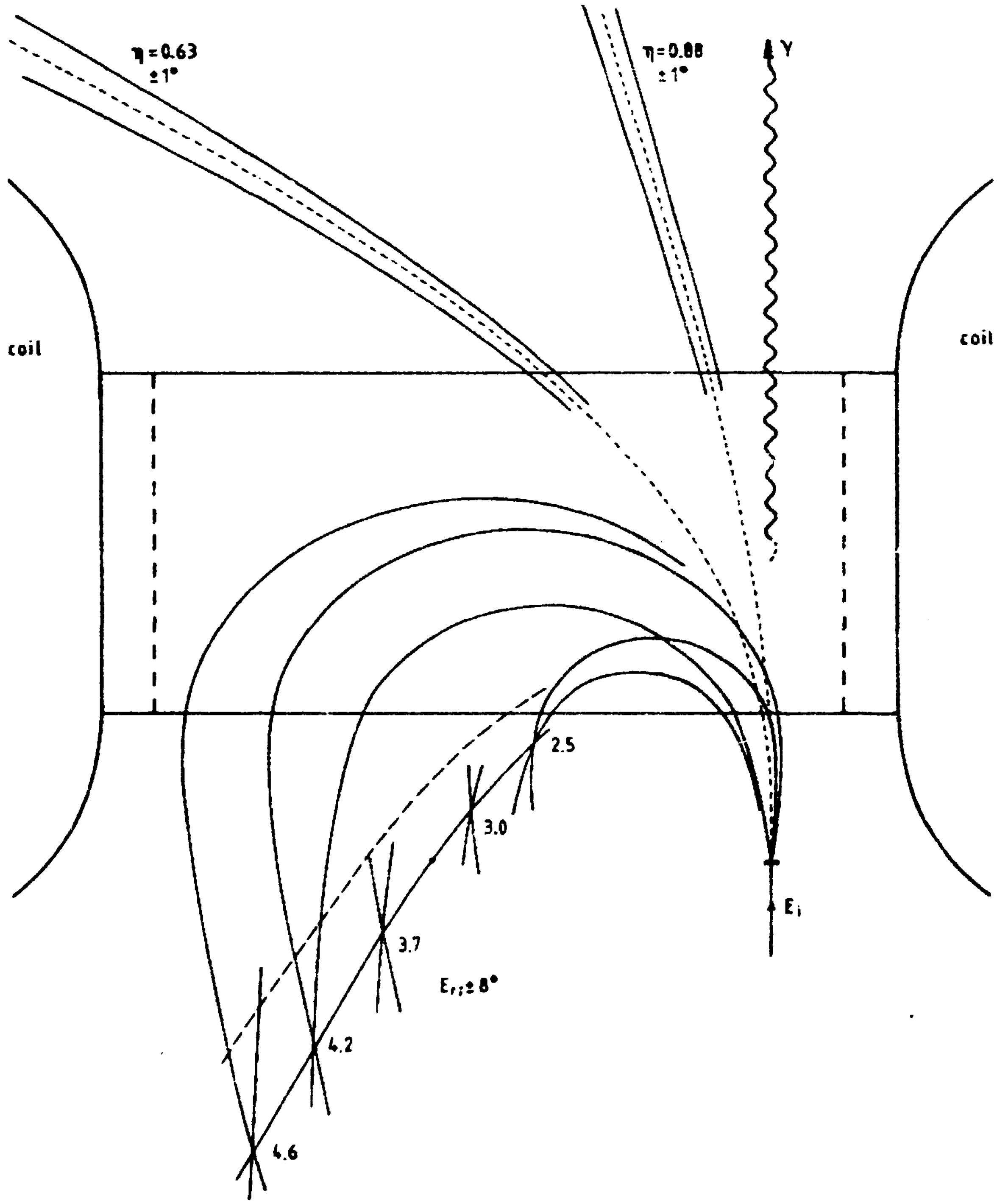

FIG. 5

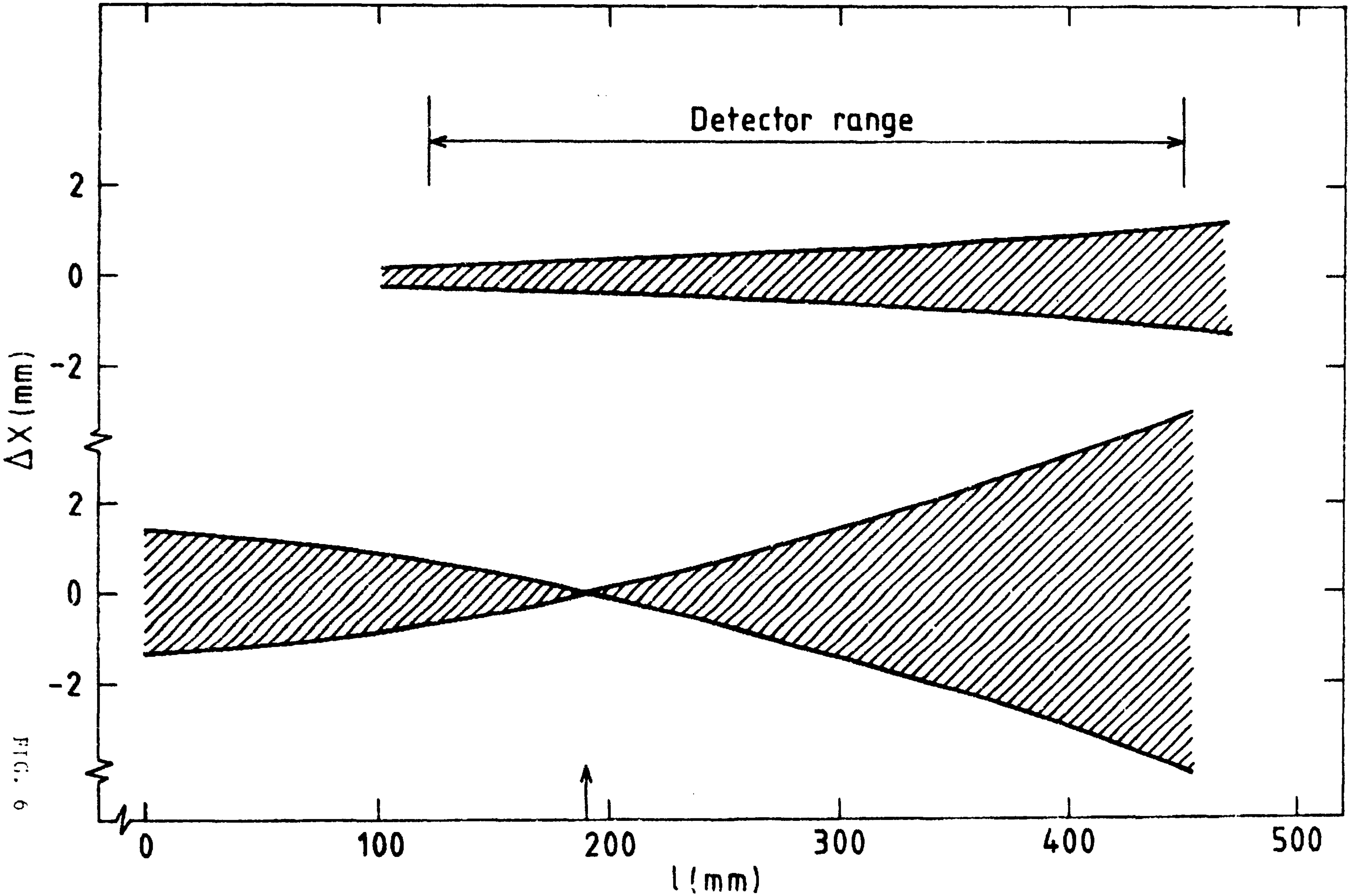

FIG. 6

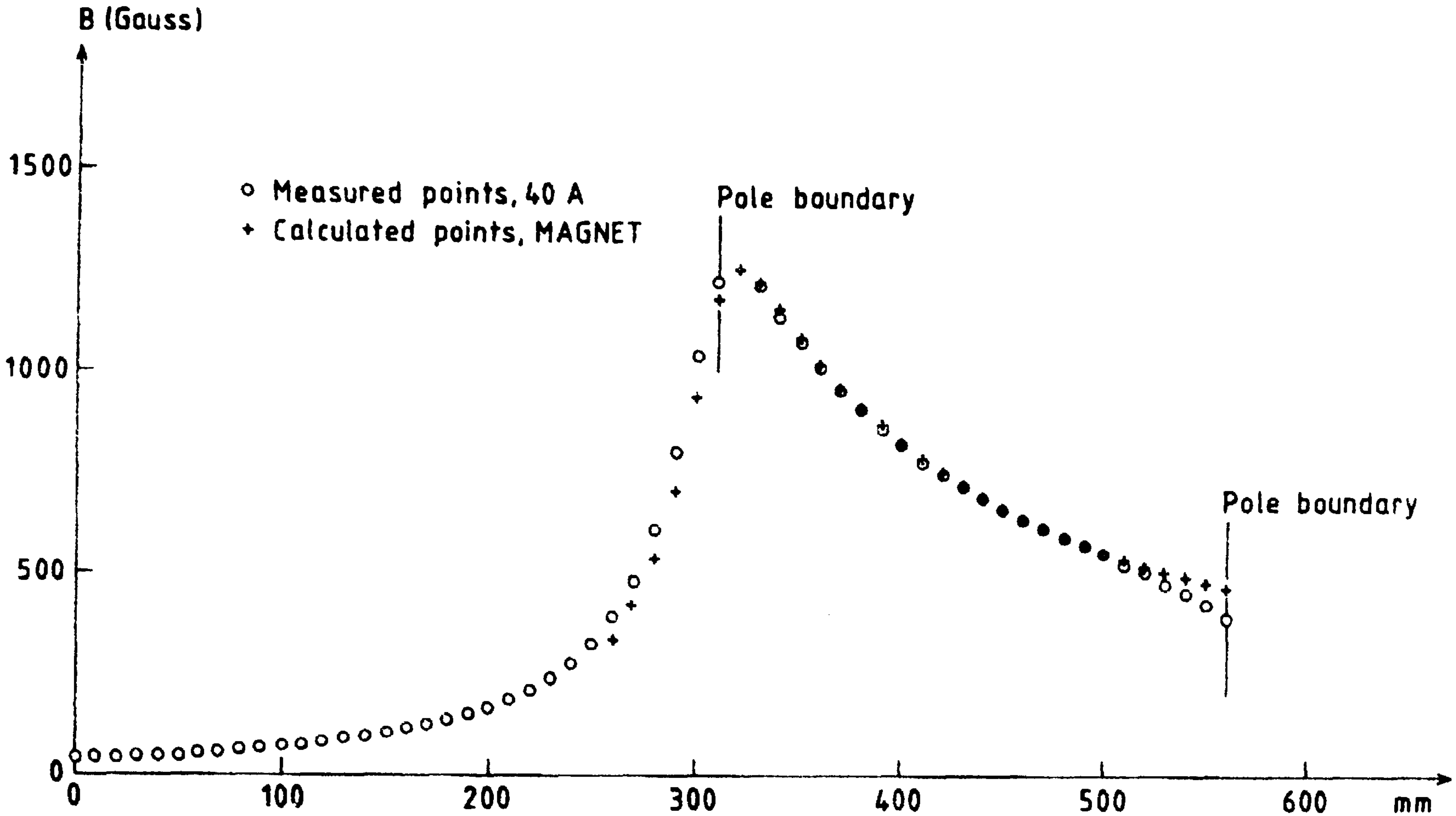
B (Gauss)
1500
1000
500
0
0
100
200
300
400
500
600
mm
○ Measured points, 40 A
+ Calculated points, MAGNET
Pole boundary
Pole boundary

FIG. 7

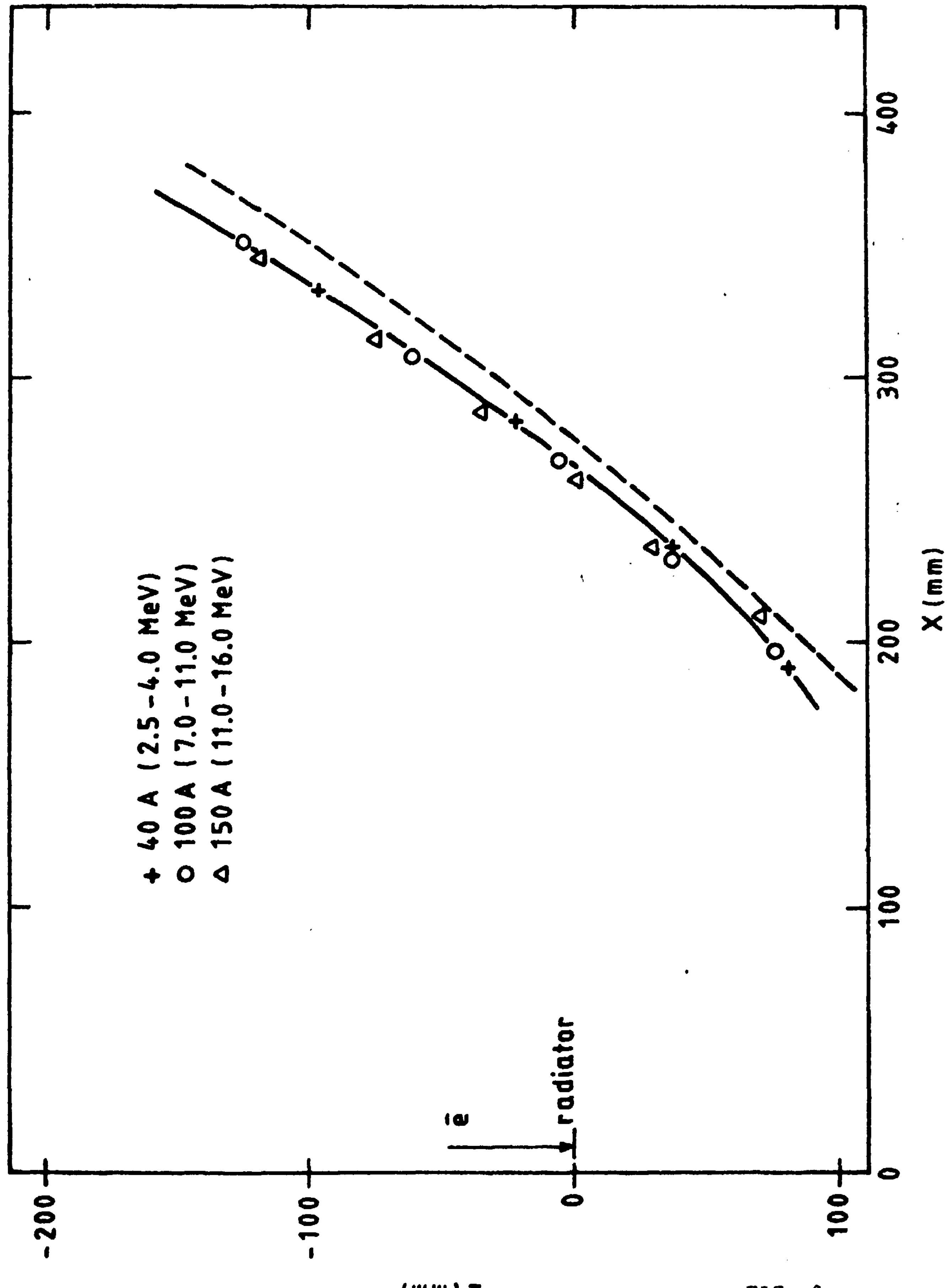

+ 40 A (2.5 - 4.0 MeV)
o 100 A (7.0 - 11.0 MeV)
Δ 150 A (11.0 - 16.0 MeV)
e
radiator
X (mm)
Z (mm)
0
100
200
300
400
-200
-100

FIG. 8

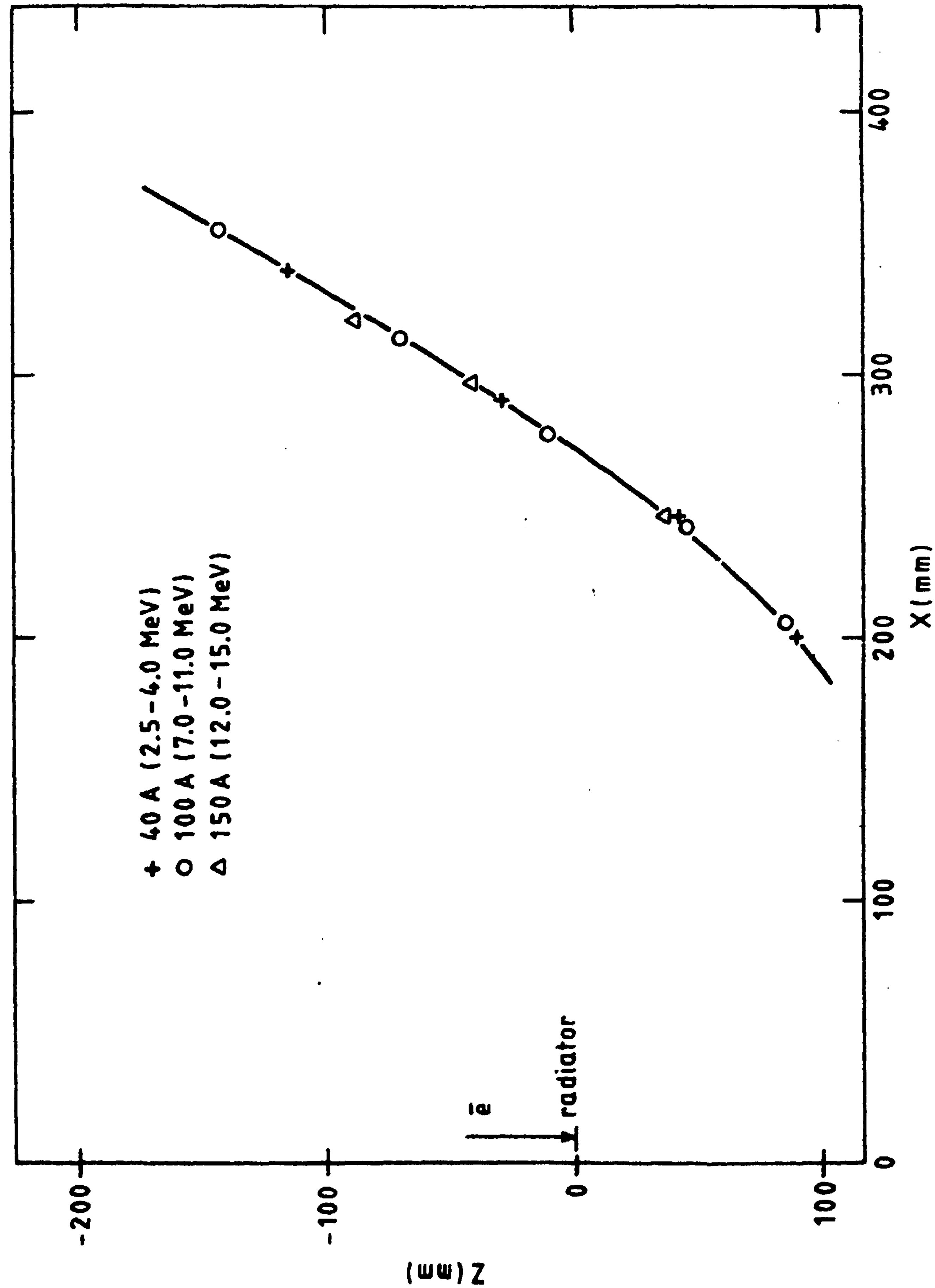

+ 40 A (2.5-4.0 MeV)
o 100 A (7.0-11.0 MeV)
Δ 150 A (12.0-15.0 MeV)
e
radiator
X (mm)
Z (mm)
0
100
200
300
400
-200
-100

FIG. 9

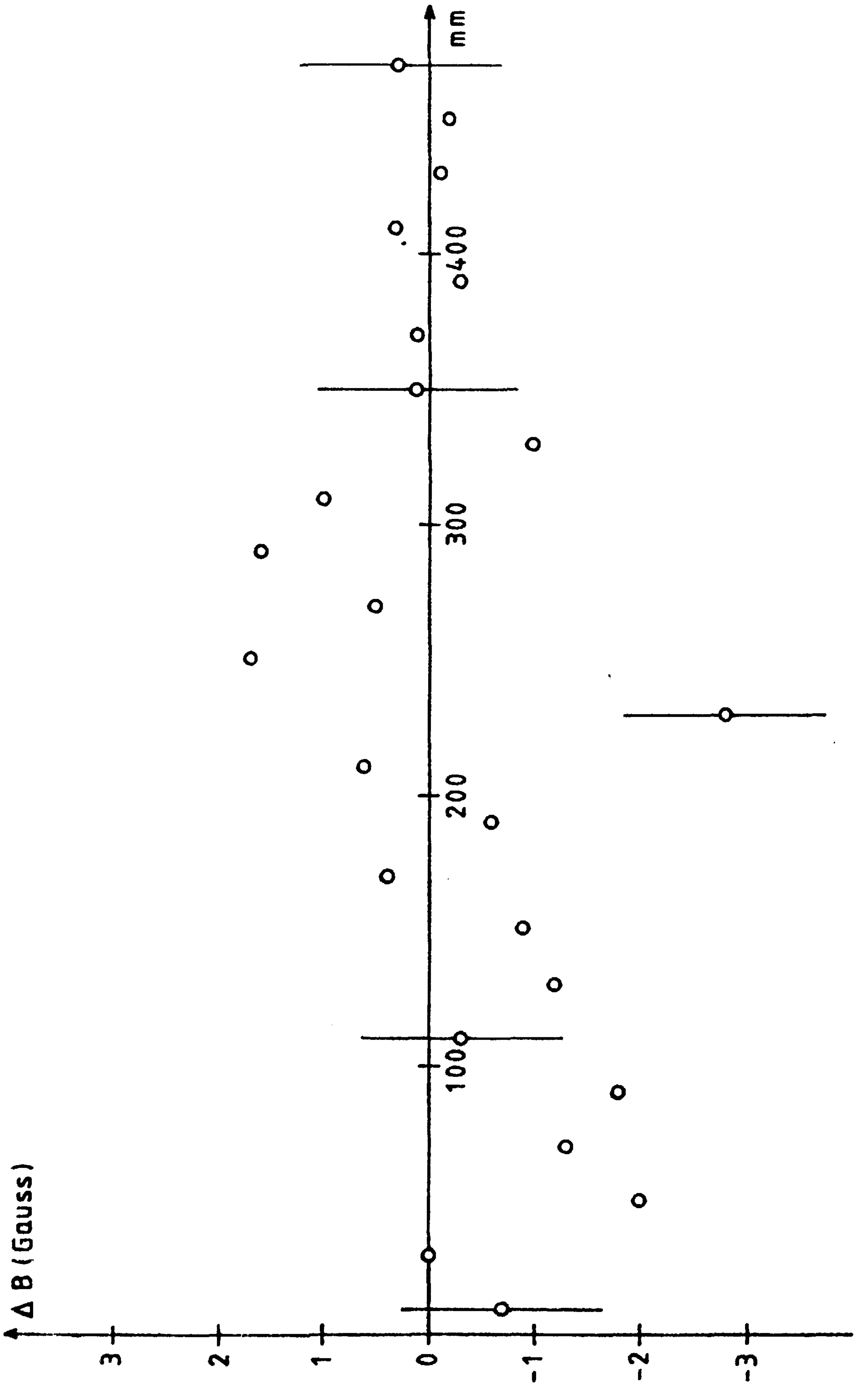

FIG.10

FIG.11

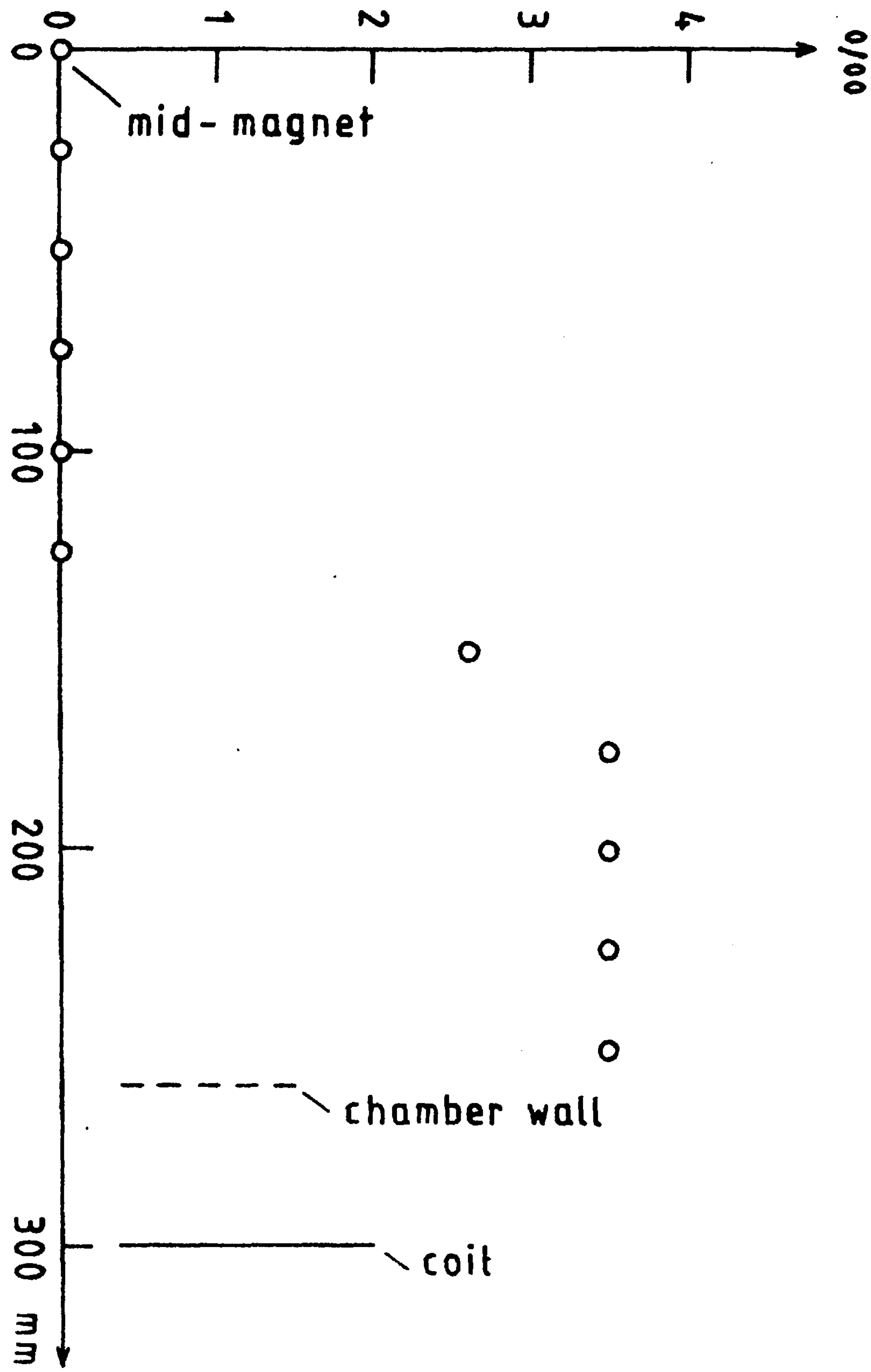

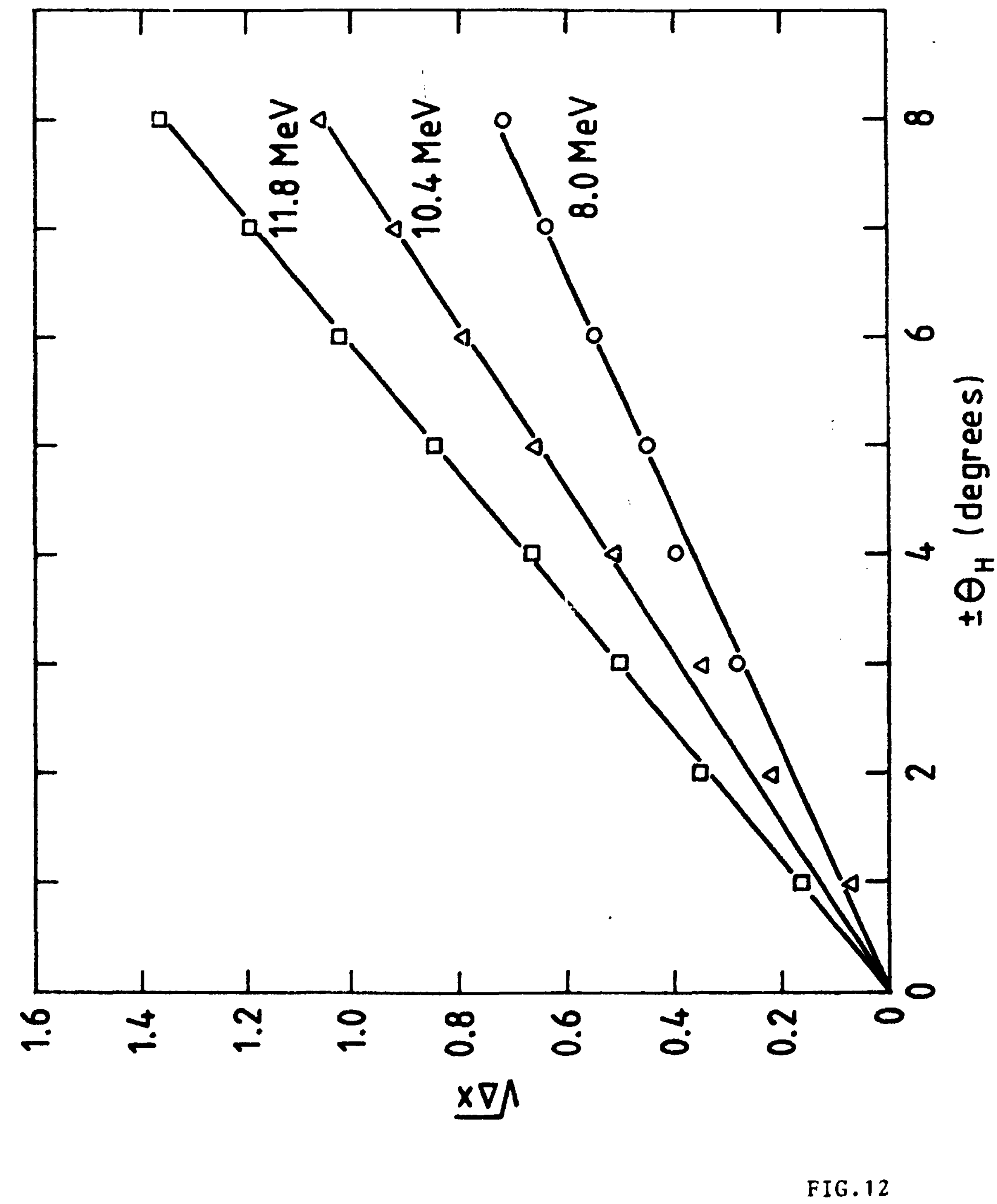

11.8 MeV
10.4 MeV
8.0 MeV
±Θ_H (degrees)
√Δx
0
2
4
6
8
0
0.2
0.4
0.6
0.8
1.0
1.2
1.4
1.6

FIG.12

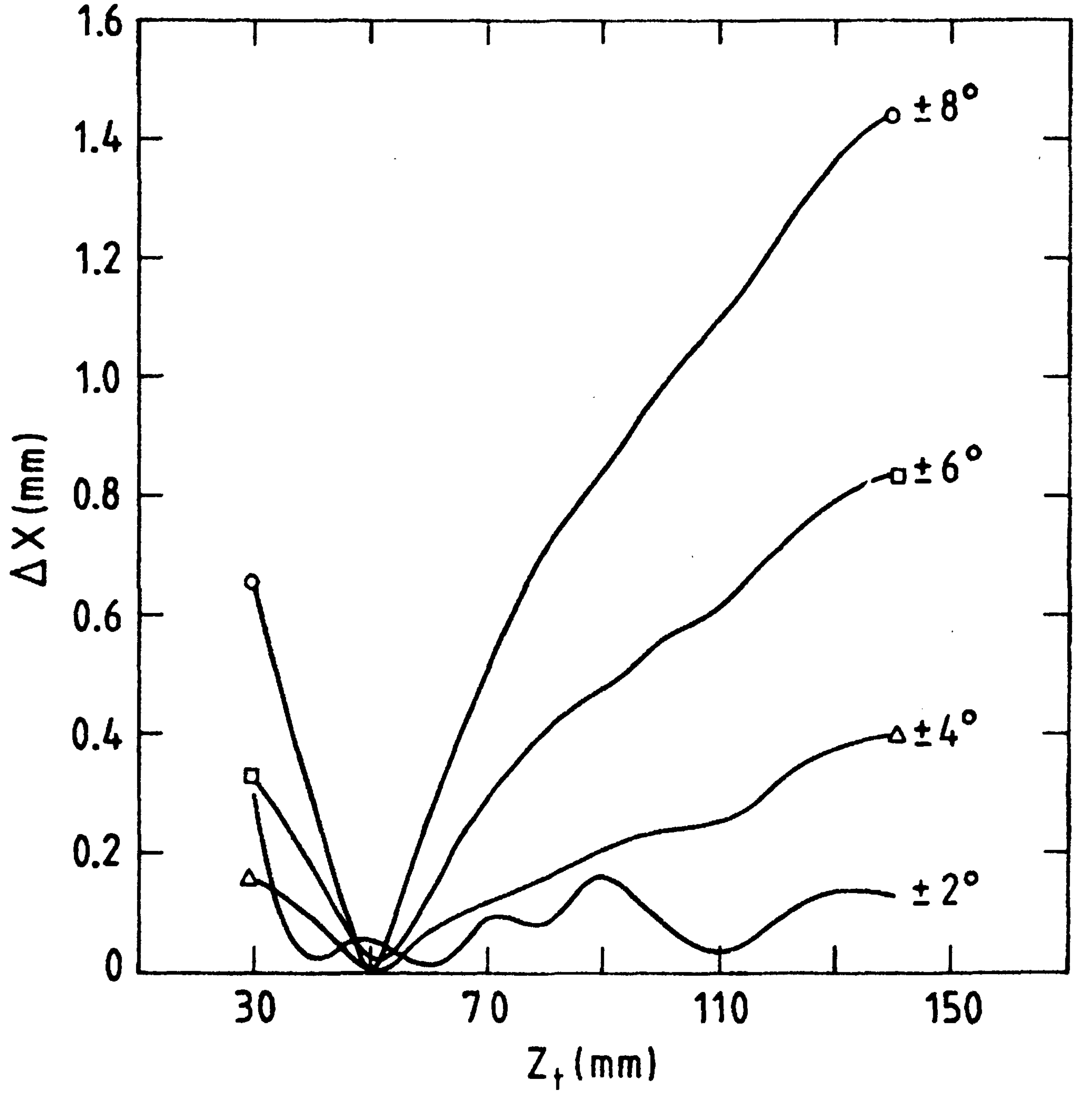

FIG. 13

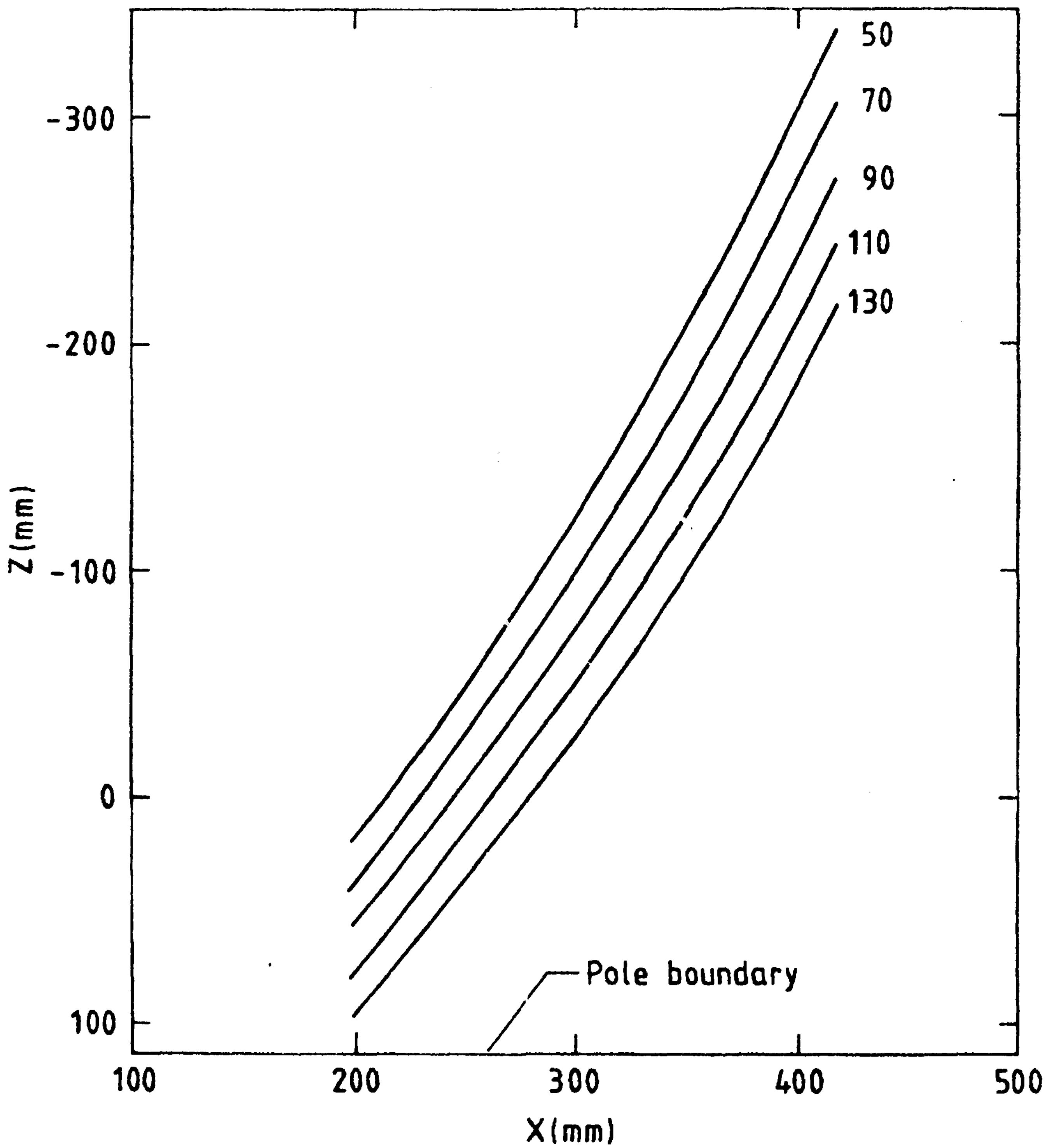
50
70
90
110
130
-300
-200
-100
0
100
Z(mm)
Pole boundary
100
200
300
400
500
X(mm)

FIG.14

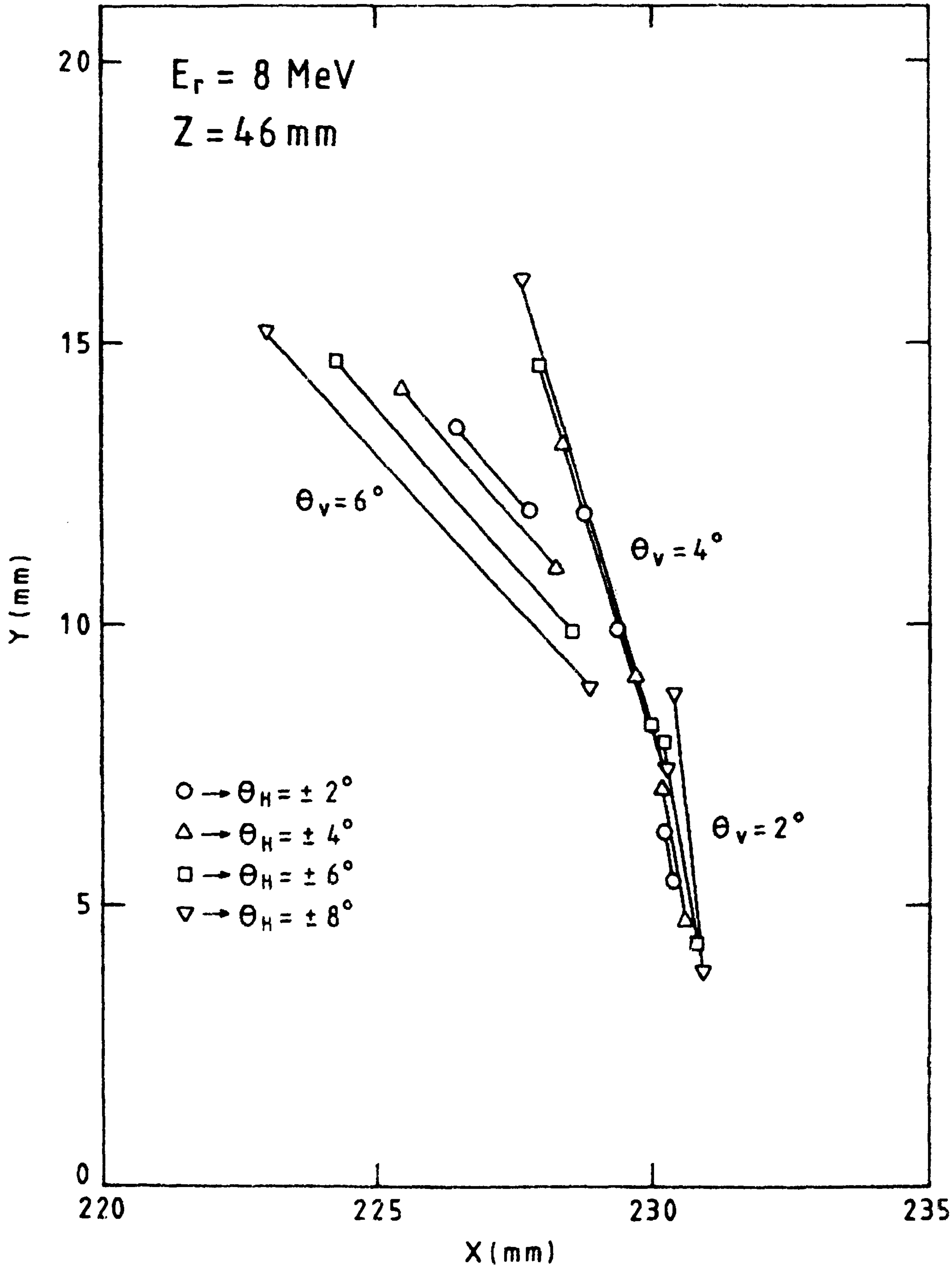
Er = 8 MeV
Z = 46 mm
θv = 6°
θv = 4°
θv = 2°
○ → θH = ± 2°
△ → θH = ± 4°
□ → θH = ± 6°
▽ → θH = ± 8°
Y (mm)
X (mm)
0
5
10
15
20
220
225
230
235

FIG.15

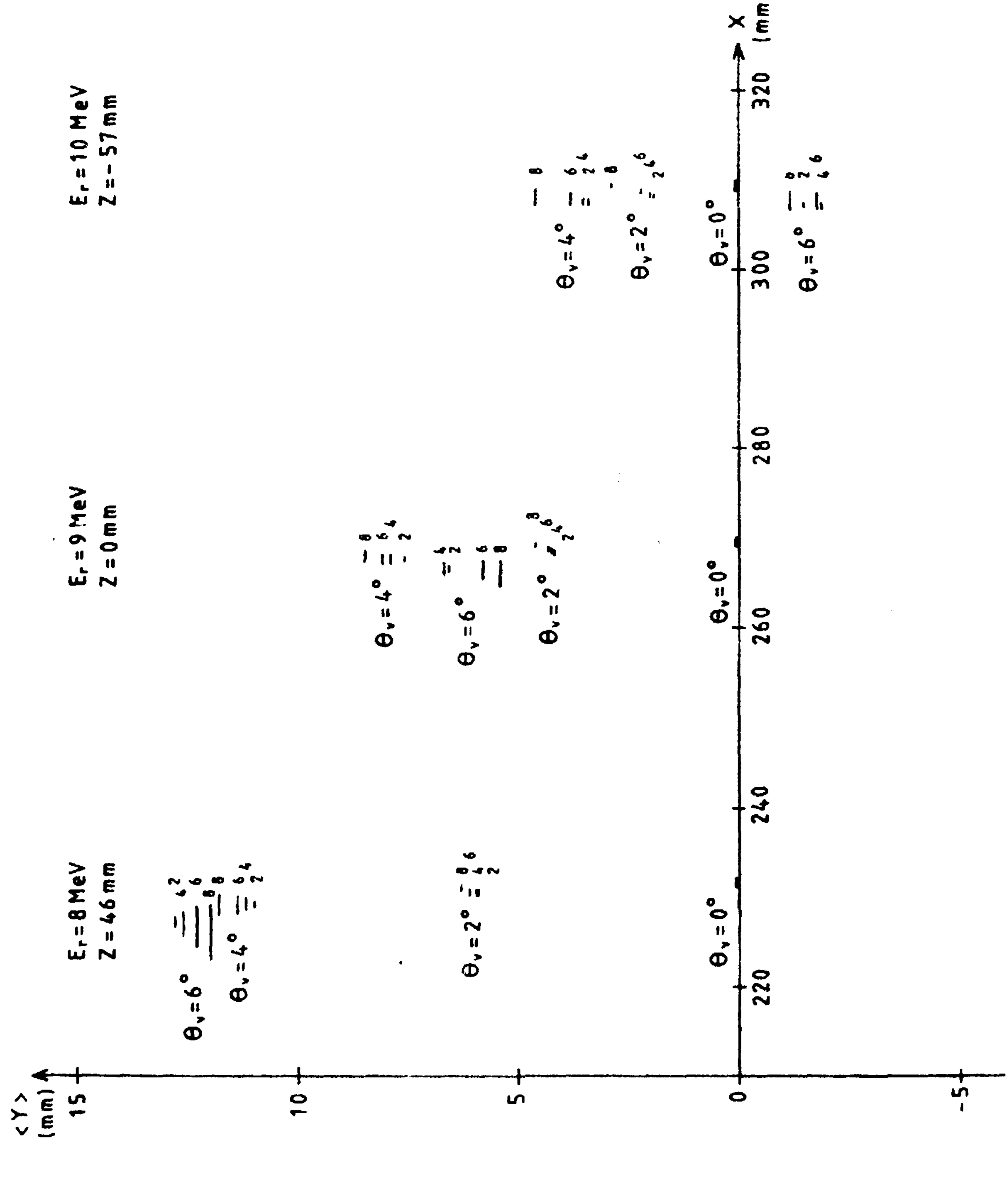

<Y> (mm)
15
10
5
0
-5
X (mm)
220
240
260
280
300
320
E_r = 8 MeV
Z = 46 mm
θ_v = 6°
θ_v = 4°
θ_v = 2°
θ_v = 0°
E_r = 9 MeV
Z = 0 mm
E_r = 10 MeV
Z = -57 mm

FIG.16

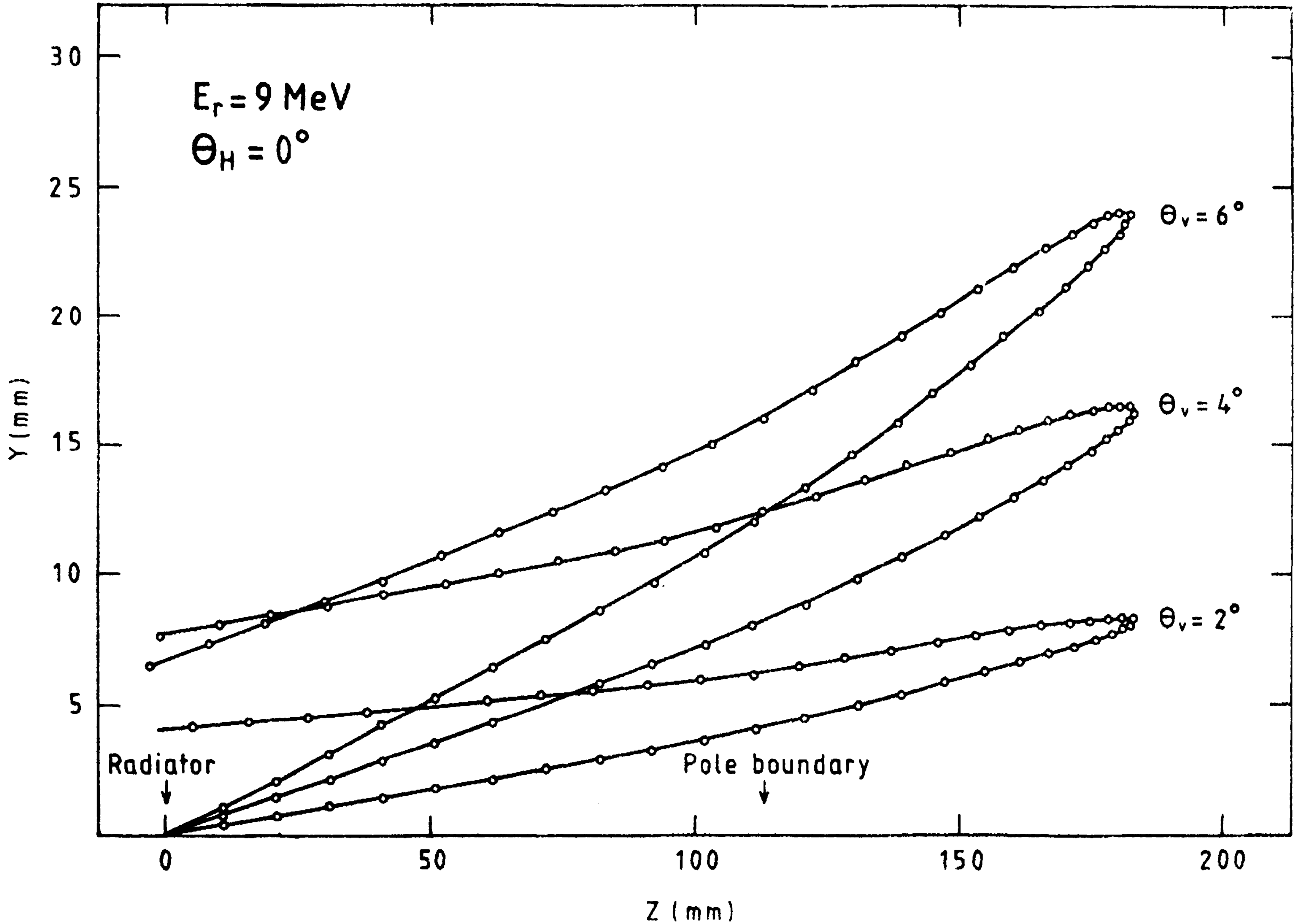

$E_r = 9$ MeV
$\Theta_H = 0°$
$\Theta_v = 6°$
$\Theta_v = 4°$
$\Theta_v = 2°$
Radiator
Pole boundary
Y (mm)
Z (mm)
30
25
20
15
10
5
0
50
100
150
200

FIG.17

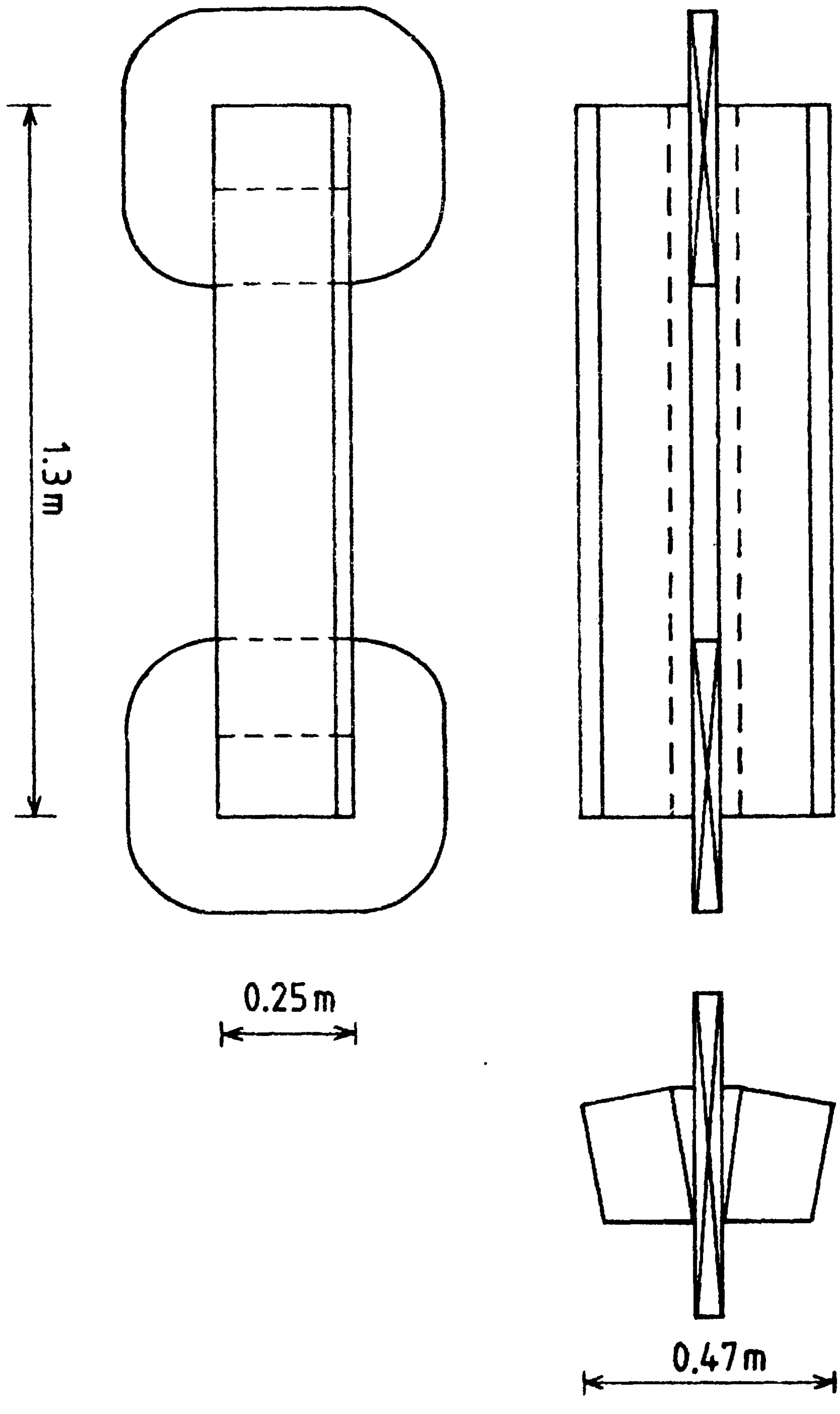

FIG.18

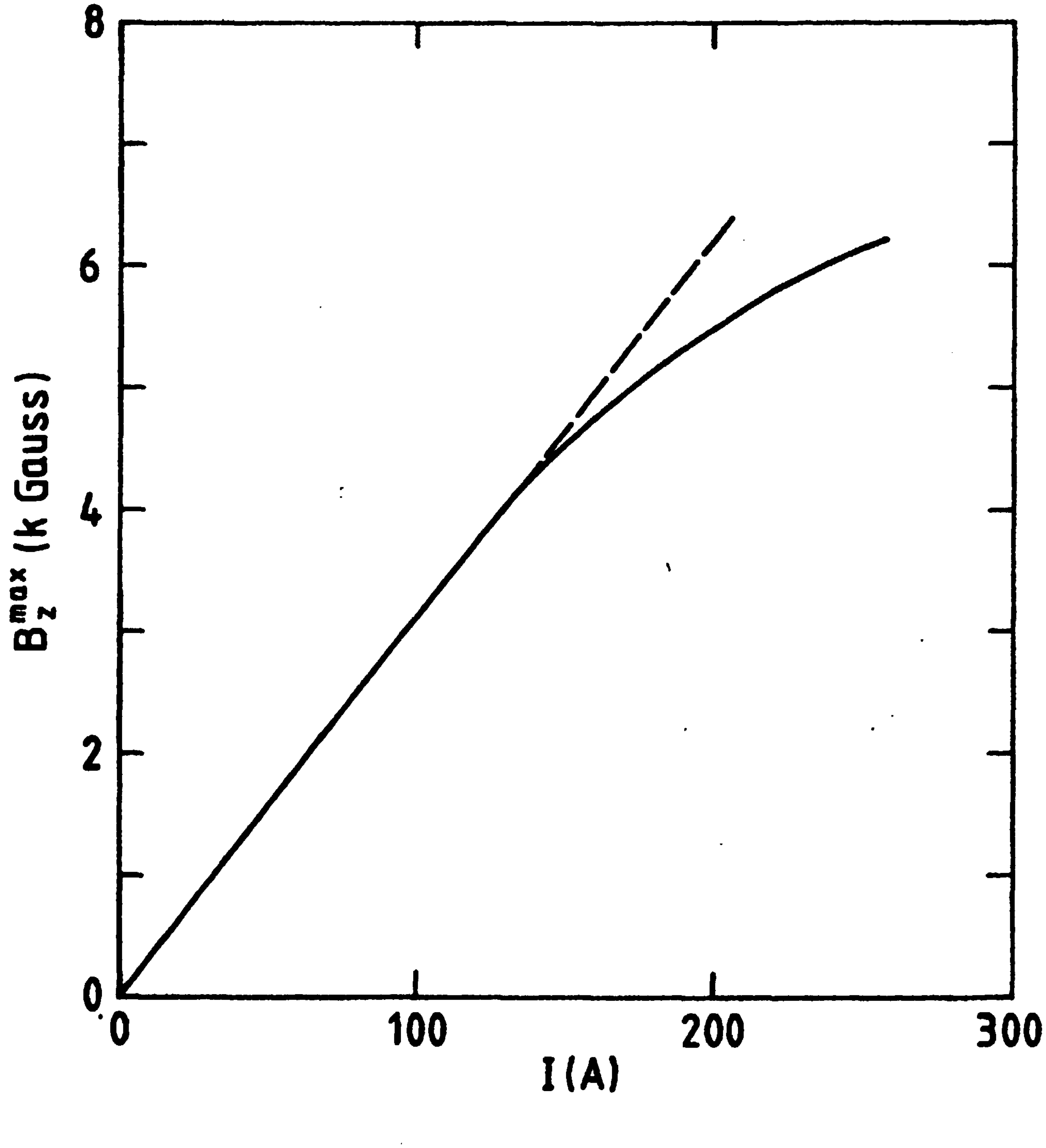

FIG.19

APPENDIX A. MAGNETIC FIELD MEASUREMENTS

In this appendix the calibration of a Hall-probe and the procedure for measuring the magnetic field in the spectrometer magnet are described. The strong variation of the field inside and outside the pole-gap made it necessary to use a Hall-probe for these measurements. The probe was temperature stabilized and it was connected to an automatic measurement system consisting of a step-motor controller and an ADC for reading measurement values via CAMAC into a computer. In order to do absolute measurements the Hall-probe had to be calibrated. This was done against a NMR-probe (B > 1 kGauss) and a flip-coil (B < 1.5 kGauss) in a homogeneous field. The calibration values for both field directions are given in tables A1 - A4, and are plotted in figures A1 - A4. As is clear from fig. A4 the overlap between the results for the flip-coil and the NMR-probe is not complete in this direction. There is a systematic deviation of 4 Gauss. This deviation was adjusted by fitting the values obtained by the flip-coil to those obtained by NMR. By doing so the straight line combining the points passed exactly through the origin of coordinates.

In our case the field points only in one direction and therefor only the +ADC values in tables A2 and A4 were used for the calibration. To all calibration points a polynomial of sixth order (B = f(+ADC) was fitted. The result of this fit is given in table A5, where the regression coefficients, input data and values calculated with the polynomial are presented. As also can be seen in table A5 the difference between input and calculated values is always less than 2.3 Gauss.

When measuring the spectrometer magnet field the probe was attached to a motor-driven sleigh movable in a grider. The grider rested on two blocks which could be moved sideways on a plane plate of glass. The magnet position was adjusted with the aid of a water-level (accuracy 0.04 mm/m) so that the front edge and gables were vertical. Then the symmetry plane of the polegap was supposed to be horizontal. The glass plate was then horizontally adjusted with an accuracy better than 0.2 mm/m. The parallellism of the glass plate in the horizontal plane with respect to the magnet was checked by moving the probe sideways. The parallellism could be checked with an accuracy of 1 mm/m. The vertical position of the probe with respect to the magnet was determined by measuring the magnetic field. Since the field lines inside the magnet are circular the Hall-voltage has a maximum when the probe lies in the median plane as the field lines than are perpendicular to the probe. Thus the maximum field defines the median plane.

The field measurements were carried out automatically with the aid of a step-motor. Measurements were done with three different currents in the coils and the step-length was 2 mm. The measured fields in the median plane at 40, 100 and 150 A current are given in tables A6-A8. The field in the X-direction was also measured, see fig. 11.

TABLE CAPTIONS (Appendix A)

Table A1 Fields measured with NMR probes and -ADC values generated by the Hall-probe at three different amplifications. The magnetization current is also given. The values marked with a star indicate ADC overflow.

Table A2 Same as table A1 but for reversed magnetic field direction.

Table A3 Fields measured with a flip-coil and -ADC values generated by the Hall-probe.

Table A4 Same as table A3 but for reversed field direction.

Table A5 Regression coefficients obtained from the fit of a polynomial of sixth order to the calibration values given in tables A2 and A4. The input field values, field values calculated with the polynomial and the difference between these two are also given.

Table A6 The field in the median plane of the spectrometer magnet measured with the Hall-probe at 40A current in the coils. The first value correspond to a position 178 mm inside the front edge. Steplength 2 mm.

Table A7 Same as table A6 but at 100 current. The first value correspond to a position 178 mm inside the front edge.

Table A8 Same as table A6 but at 150 A current. The first value correspond to a position 311 mm outside the front edge.

TABLE A1

Probe	I (A)	B(Gauss)	-ADC (HALL)		
NMR			x 1	x 3	x 10
2	60.0	1047.7	386	1162	3870
	65.0	1128.7	416	1252	4173
	70.0	1208.6	446	1342	4474
	75.0	1293.1	478	1438	4793
	85.0	1465.1	544	1634	5445
	90.1	1554.4	578	1738	5786
	100.0	1722.7	642	1930	6431
	150.2	2590.5	984	2954	8202*
3	150.3	2592.3	985	2956	
	200.0	3454.1	1340	4018	
	250.0	4320.7	1708	5122	
	300.0	5191.3	2096	6283	
4	300.1	5192.4	2096	6286	
	350.0	6058.0	2488	7460	
	400.0	6926.0	2888	8201*	
	449.8	7789.0	3292		
	500.1	8663.0	3704		
	550.1	9549.0	4126		
	600.1	10383.0	4524		
5	600.0	10408.0	4536		
	650.1	11236.0	4932		
	700.0	12063.0	5330		
	750.0	12874.0	5718		
	800.0	13642.0	6088		
	850.0	14340.0	6418		
	900.0	14963.0	6713		
	950.0	15516.0	6976		
	1000.0	16023.0	7214		

TABLE A2

Probe	I (A)	B(Gauss)	ADC (HALL)		
NMR			x 1	x 3	x 10
2	55.0	987.9	366	1095	3650
	60.0	1067.4	395	1182	3946
	70.0	1231.9	456	1368	4562
	80.0	1400.9	520	1558	5180
	90.0	1566.0	584	1748	5827
	100.0	1734.6	648	1942	6471
	150.0	2592.2	984	2950	8178*
3	150.0	2592.0	984	2950	
	200.0	3457.1	1340	4014	
	250.0	4321.2	1708	5117	
	300.0	5191.7	2090	6262	
4	299.9	5191.4	2090	6262	
	350.0	6054.1	2478	7428	
	400.0	6925.0	2878	8182*	
	450.0	7787.7	3278		
	500.0	8660.2	3688		
	550.0	9516.3	4088		
	600.0	10378.5	4499		
5	600.0	10378.2	4499		
	650.0	11228.6	4903		
	700.0	12063.8	5300		
	750.0	12883.2	5688		
	800.0	13652.5	6053		
	850.0	14338.1	6376		
	900.0	14963.2	6670		
	950.0	15518.0	6931		
	999.2	16014.0	7160		

TABLE A3

B_{coil} (Gauss)	- ADC (x 3)
24.1	24
54.3	56
86.6	90
118.5	126
150.7	161
183.2	197
213.8	232
245.5	266
277.4	300
309.3	336
340.6	370
494.5	540
582.9	638
642.8	704
707.5	776
770.1	845
822.3	904
895.3	984
964.1	1064
1015.8	1120
1126.3	1244
1209.4	1338
1340.5	1486
1482.1	1648

0-level corresponds to ADC = 8184

TABLE A4

B_{coil} (Gauss)	ADC (x 3)
23.5	28
72.7	82
134.5	150
207.4	230
273.6	302
324.9	360
398.4	440
454.4	502
511.4	564
568.5	628
642.3	710
709.3	784
766.3	847
828.9	916
896.3	992
953.9	1056
1021.4	1132
1089.8	1208
1184.3	1314
1282.9	1424
1377.5	1532
1479.5	1648

0-level corresponds to ADC = 8184

TABLE A5

INTERCEPT AND REGRESSION COEFFICIENTS

-1.8487E-01	9.1139E-01	-1.5950E-06	-5.1015E-09
7.3148E-13	-3.3748E-17		

INPUT Y-VALUES AND FITTED POLYNOM AND DIFFERENCE

6.0541E+03	6.0545E+03	-4.0910E-01
5.1914E+03	5.1915E+03	-1.2127E-01
4.3212E+03	4.3212E+03	-2.3685E-02
3.4571E+03	3.4572E+03	-1.2577E-01
2.5920E+03	2.5914E+03	5.7500E-01
1.7346E+03	1.7358E+03	-1.2278E+00
1.5660E+03	1.5679E+03	-1.9557E+00
1.4009E+03	1.4014E+03	-5.7576E-01
1.2319E+03	1.2329E+03	-1.0516E+00
1.0674E+03	1.0686E+03	-1.2659E+00
9.8790E+02	9.9017E+02	-2.2755E+00
1.4795E+03	1.4778E+03	1.6468E+00
1.3775E+03	1.3759E+03	1.5376E+00
1.2829E+03	1.2807E+03	2.1874E+00
1.1843E+03	1.1833E+03	9.7154E-01
1.0898E+03	1.0891E+03	6.5514E-01
1.0214E+03	1.0214E+03	-1.8948E-02
9.5390E+02	9.5353E+02	3.6602E-01
8.9630E+02	8.9624E+02	5.1223E-02
8.2890E+02	8.2808E+02	8.1294E-01
7.6630E+02	7.6608E+02	2.1858E-01
7.0930E+02	7.0937E+02	-7.1007E-02
6.4230E+02	6.4264E+02	-3.4721E-01
5.6850E+02	5.6857E+02	-7.8015E-02
5.1140E+02	5.1067E+02	7.2176E-01
4.5440E+02	4.5451E+02	-1.1849E-01
3.9840E+02	3.9829E+02	1.0420E-01
3.2490E+02	3.2566E+02	-7.6618E-01
2.7360E+02	2.7295E+02	6.4322E-01
2.0740E+02	2.0747E+02	-7.0697E-02
1.3450E+02	1.3464E+02	-1.4976E-01
7.2700E+01	7.2713E+01	-1.3563E-02
2.3500E+01	2.3510E+01	-1.0107E-02
0.0000E+00	-1.8487E-01	1.8487E-01

TABLE A6

377.424	383.777	390.130	397.388	402.832
410.089	416.439	422.787	428.228	435.482
440.922	446.361	452.706	457.237	463.581
468.112	474.454	478.983	484.418	489.852
493.475	498.908	504.341	507.962	513.394
515.204	522.445	526.065	529.685	535.114
539.638	544.161	547.779	551.397	556.823
560.440	564.057	569.482	573.098	576.714
580.330	585.752	590.271	594.788	598.402
602.016	605.629	611.049	616.467	620.079
623.691	630.011	634.524	638.135	643.550
648.964	652.573	659.790	663.398	668.810
674.220	679.630	685.039	688.645	695.855
703.064	708.470	713.875	721.080	726.484
731.886	739.088	745.388	751.687	758.885
766.081	773.276	778.671	785.864	794.852
802.041	809.228	816.414	824.496	832.576
839.756	849.627	857.701	866.670	875.636
884.600	893.561	902.520	911.476	918.638
932.959	943.696	953.534	964.263	975.882
986.603	997.320	1009.818	1022.311	1033.015
1047.281	1059.757	1072.229	1086.475	1099.824
1113.166	1125.613	1139.831	1154.042	1168.246
1184.215	1196.630	1210.810	1224.983	1235.607
1246.228	1255.959	1260.381	1263.918	1260.381
1256.843	1244.458	1224.983	1200.175	1168.246
1130.946	1088.255	1040.149	992.855	943.696
893.561	846.936	800.243	757.086	716.577
677.827	643.550	609.242	580.330	551.397
526.065	500.719	478.983	457.237	439.109
420.973	404.647	390.130	375.609	361.084
348.372	336.566	324.758	312.038	304.769
293.864	282.957	275.684	268.411	261.137
253.862	246.587	239.311	233.854	224.757
221.118	216.569	210.200	205.651	201.101
195.641	192.001	186.540	181.080	179.259
173.798	170.157	166.516	163.785	159.233
157.412	153.771	151.039	148.308	144.666
142.845	137.382	137.382	133.739	131.918
130.097	126.454	124.633	122.811	120.990
118.258	115.526	114.615	111.883	108.240
108.240	107.329	104.596	103.685	100.953
100.042	99.131	97.309	95.488	93.666
92.755	91.844	90.022	88.200	86.378
85.468	84.557	82.735	82.735	79.091
79.091	79.091	77.269	76.358	75.447
74.536	71.803	71.803	71.803	69.980
69.980	68.158	68.158	66.336	64.514
64.514	64.514	63.603	62.692	60.870
60.870	60.870	59.047	57.225	57.225
57.225	57.225	55.403	55.403	54.492
53.581	53.581	49.936	49.936	49.936
49.936	49.936	49.936	49.936	48.114
48.114	48.114	46.291	46.291	46.291
46.291	44.469	44.469	42.646	42.646
42.646	42.646	42.646	41.735	40.824
40.824	40.824	39.002	39.002	39.002

TABLE A7

1490.997	1502.582	1513.761	1524.261	1536.504
1546.993	1559.223	1569.702	1582.793	1595.877
1607.210	1618.537	1632.471	1645.526	1658.573
1670.743	1684.644	1698.536	1712.420	1726.294
1740.160	1754.017	1769.595	1784.298	1798.991
1814.537	1830.071	1846.457	1862.830	1878.329
1895.537	1912.732	1929.912	1948.794	1966.802
1984.794	2003.627	2022.442	2039.532	2063.434
2083.900	2104.345	2124.770	2146.873	2168.953
2191.009	2213.041	2236.741	2262.103	2284.058
2311.046	2336.315	2361.552	2388.437	2415.286
2443.773	2472.220	2502.297	2531.494	2562.314
2592.256	2625.472	2657.805	2690.086	2724.793
2757.791	2790.736	2826.913	2862.206	2895.801
2933.427	2967.721	3000.330	3032.887	3062.144
3088.117	3110.816	3125.396	3132.682	3128.634
3114.057	3083.249	3037.766	2974.247	2895.801
2800.609	2695.048	2578.954	2458.838	2336.315
2214.735	2094.125	1983.081	1874.886	1774.786
1680.301	1592.389	1512.011	1436.622	1366.278
1302.794	1242.688	1187.763	1136.278	1088.255
1043.715	1003.570	965.157	928.485	893.561
861.289	832.576	803.837	778.671	753.487
730.085	706.668	686.842	666.104	645.354
629.108	611.049	594.788	578.522	564.057
549.588	535.114	522.445	509.773	497.097
486.230	474.454	463.581	453.612	442.735
433.669	424.601	413.718	406.461	398.296
390.130	381.054	373.793	366.531	359.269
352.005	346.556	339.291	333.841	326.575
321.124	315.673	310.221	304.769	297.499
293.864	288.410	282.957	279.320	274.775
268.411	264.774	261.137	257.500	252.953
248.406	244.768	239.311	237.492	233.854
230.215	224.757	222.938	219.299	216.569
213.840	210.200	206.561	202.921	201.101
198.371	195.641	192.001	190.181	187.451
184.720	181.080	180.169	177.439	173.798
172.888	170.157	166.516	166.516	164.695
161.964	159.233	157.412	155.591	151.950
151.950	150.129	148.308	146.487	144.666
142.845	141.024	137.382	137.382	135.560
133.739	132.829	130.097	130.097	128.275
126.454	125.543	122.811	122.811	120.990
119.169	118.258	115.526	115.526	113.704
113.704	111.883	108.240	108.240	180.240
107.329	106.418	104.596	103.685	102.775
100.953	100.953	99.131	97.309	97.309

TABLE A8

142.845	144.666	146.487	148.308	149.218
151.039	151.950	153.771	155.591	157.412
159.233	161.054	162.874	164.695	166.516
166.516	170.157	171.977	173.798	175.618
177.439	180.169	181.080	184.720	186.540
188.361	191.091	193.821	195.641	195.641
199.281	202.921	204.741	206.561	210.200
212.930	215.659	217.479	221.118	223.847
224.757	228.396	232.034	235.673	238.402
241.130	244.768	246.587	250.225	253.862
257.500	261.137	264.774	268.411	272.048
275.684	279.320	282.957	288.410	292.046
296.590	301.134	304.769	310.221	314.764
319.307	324.738	329.300	333.841	339.291
344.740	348.371	355.637	361.084	366.531
372.886	379.239	384.685	391.944	398.296
404.647	411.904	419.160	426.415	433.669
441.828	449.987	457.237	466.299	475.360
484.418	493.475	500.719	511.583	522.445
532.399	543.256	554.110	565.866	576.714
589.367	602.016	614.661	629.108	642.647
657.986	672.417	688.645	703.064	721.080
739.088	757.086	775.075	796.649	818.210
839.756	861.289	886.392	911.476	938.328
965.157	993.745	1025.880	1057.975	1090.035
1128.280	1166.471	1207.266	1249.767	1295.730
1345.135	1397.958	1454.176	1513.761	1576.685
1646.396	1721.062	1800.718	1886.935	1980.512
2080.490	2189.313	2307.675	2434.561	2570.636
2716.335	2872.045	3036.139	3262.984	3381.342
3559.861	3735.432	3903.477	4057.973	4196.102
4310.432	4402.802	4470.557	4513.270	4537.764
4543.885	4534.703	4513.270	4482.624	4445.809
4402.802	4356.653	4307.348	4257.959	4205.390
4154.271	4103.058	4053.304	4003.457	3953.516
3905.042	3856.476	3809.337	3763.781	3718.091
3673.893	3631.987	3590.007	3547.156	3508.203
3469.184	3430.097	3392.541	3355.723	3318.842
3283.507	3248.919	3214.276	3181.999	3148.864
3117.297	3084.872	3054.834	3024.752	2995.442
2966.090	2938.330	2908.896	2882.698	2855.645
2829.378	2803.899	2777.565	2751.196	2728.095
2704.142	2680.159	2656.977	2632.109	2612.192
2588.931	2568.140	2545.661	2525.658	2504.801
2483.922	2463.858	2444.610	2425.345	2405.222
2386.758	2368.277	2349.779	2331.264	2313.575
2295.870	2278.994	2261.258	2243.507	2228.280
2211.347	2196.096	2196.096	2196.096	2196.096

FIGURE CAPTIONS (Appendix A)

Fig. A1 Correlation between the Hall-probe ADC values and the field measured by NMR

Fig. A2 Correlation between the Hall-probe ADC values and the field measured by flip-coil.

Fig. A3 The overlap between fields measured with NMR and flip-coil for a certain field direction (+ADC).

Fig. A4 Same as fig. A3 but for reversed field direction.

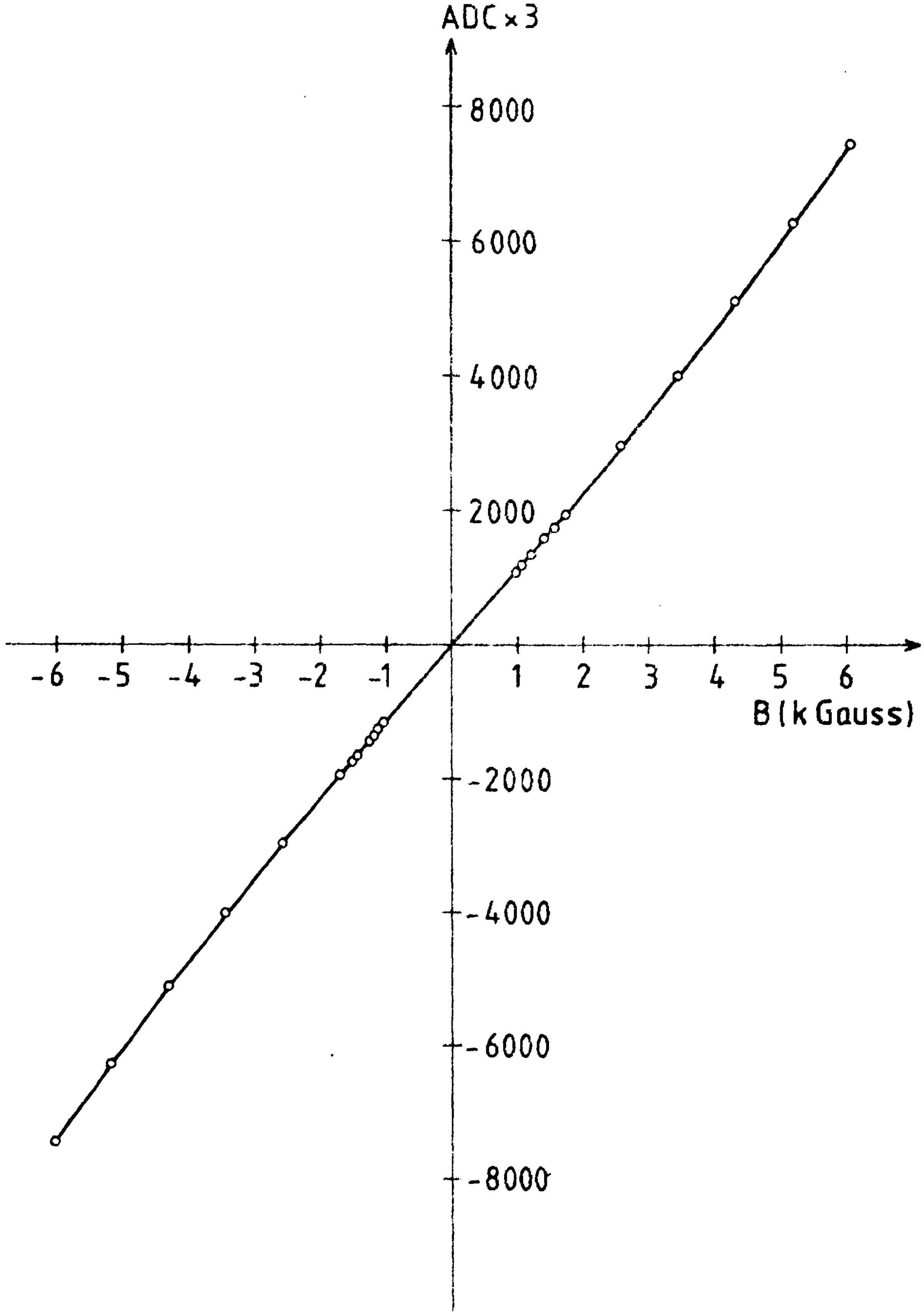
ADC×3
8000
6000
4000
2000
-2000
-4000
-6000
-8000
-6 -5 -4 -3 -2 -1 1 2 3 4 5 6
B (k Gauss)

FIG. A1

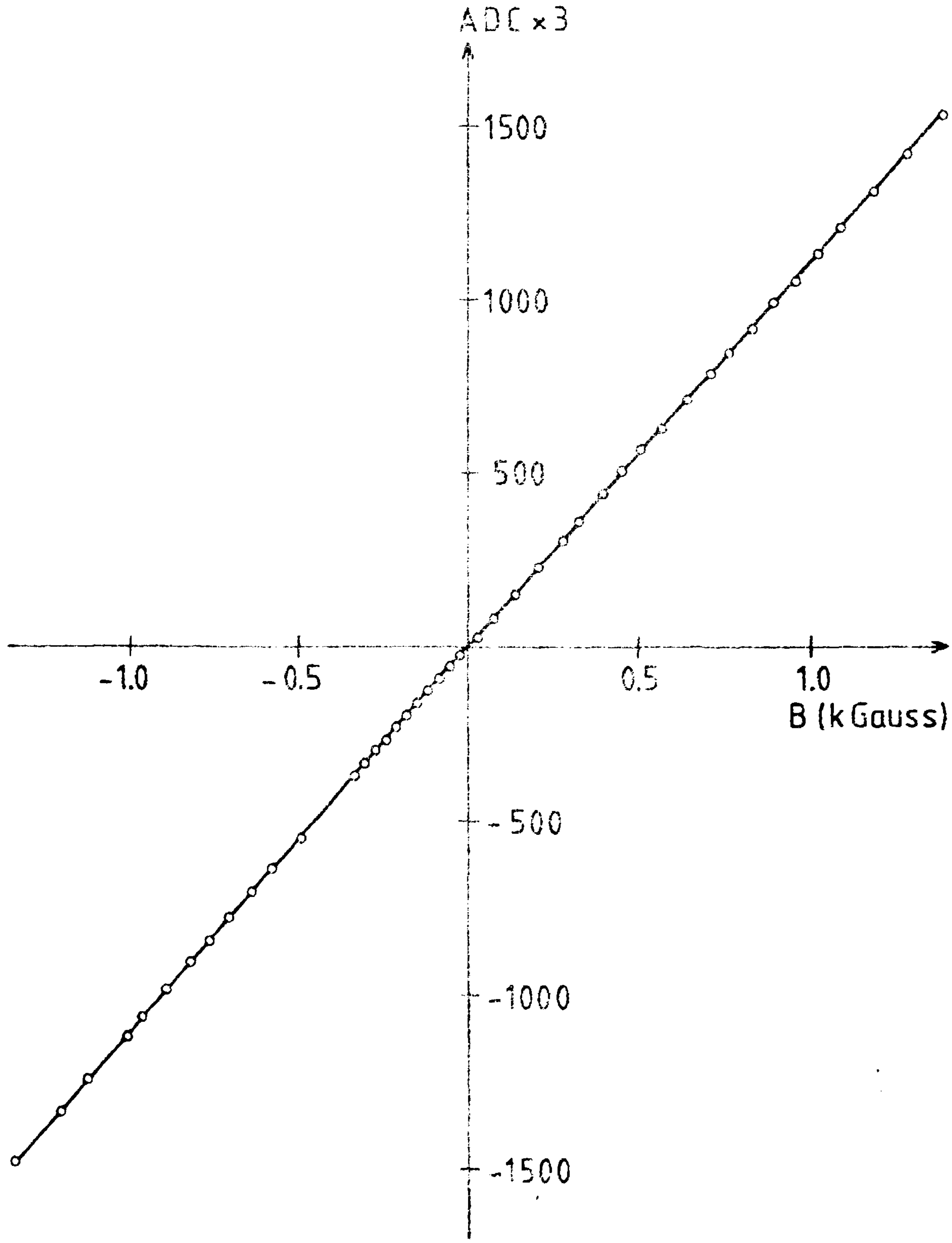

FIG. A2

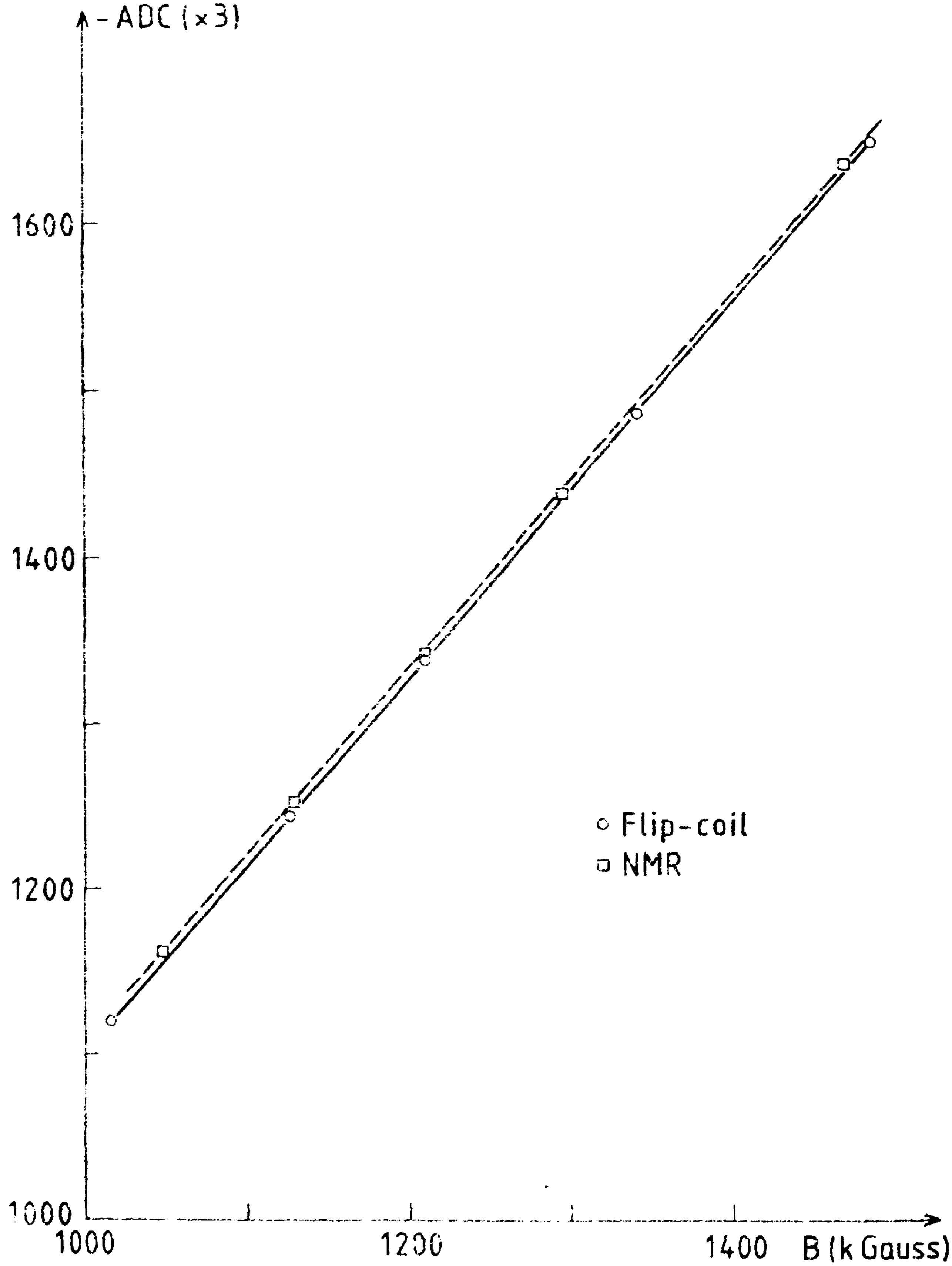
- ADC (×3)
1600
1400
1200
1000
1000
1200
1400
B (k Gauss)
○ Flip-coil
□ NMR

FIG. A3

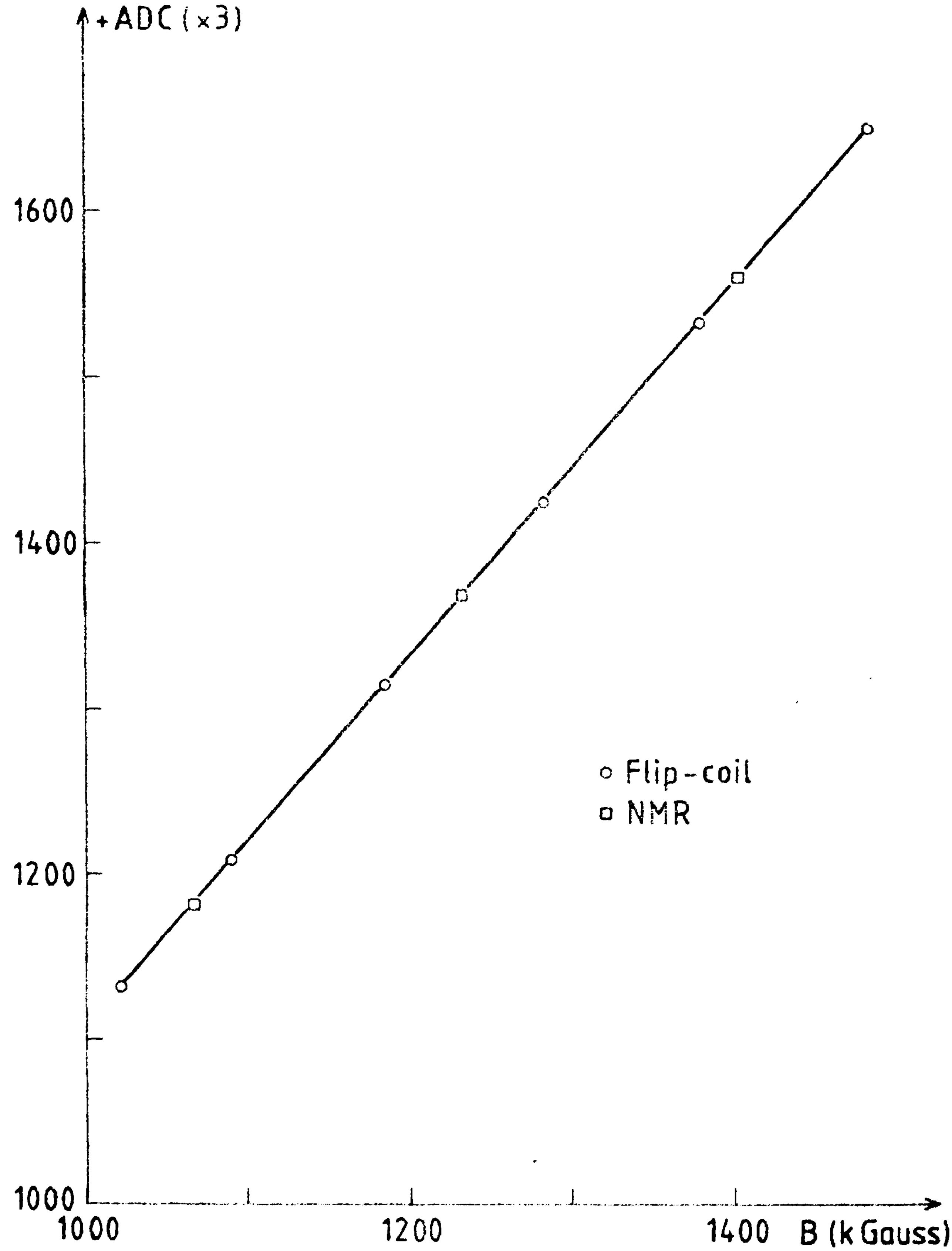

+ADC (×3)
1600
1400
1200
1000
1000
1200
1400
B (k Gauss)
○ Flip-coil
□ NMR

FIG. A4

APPENDIX B. TAYLOR EXPANSION OF MEDIAN PLANE FIELD

In this appendix the Taylor expansion of the measured field map in the median plan into a two-dimensional field-map out of this plan will be described. If a coordinate system is introduced as in fig. 4 one can Taylor expand the field components as;

$$B_X(Y,Z) = 0$$

(1) $$B_Y(Y,Z) = B_0 - B_2 + \text{higher order terms}$$

$$B_Z(Y,Z) = B_1 - B_3 + \text{higher order terms}$$

where

(2) $$B_n = B^{(n)} \quad (Z)*Y^n/n!$$

and

$$B^{(n)} = d^n B_Y(0, Z)/dZ^n$$

$B^{(n)}$ can be calculated numerically from the measured values, $B_Y(0,Z)$. These derivatives can be expressed as;

$$B^{(1)}(Z_0) = (1/2h)*(B(0,Z_1) - \quad (0,Z_{-1}) - (d_1^2-d_{-1}^2)*1/6 +$$

$$+ (d_1^4-d_{-1}^4)*1/30 + \text{higher order terms}$$

where

h = distance between measured points.

$B(0,Z_1)$ = measured value in the point $Z_0 + h$

$B(0,Z_{-1})$ = measured value in the point $Z_0 - h$

d_1^2 = second difference of the measured values in the point $Z_0 + h$

d_{-1}^4 = fourth difference of the measured values in the point $Z_0 - h$.

With the same notation as above the higher derivatives of $B(Z_0)$ can be written;

$$B^{(2)}(Z_0) = (1/h^2)*\{d_0^2 - d_0^4/12 + d_0^6/90 + \text{higher order terms}\}$$

where

d_0^2 = the second difference in the point Z_0

and

$$B^{(3)}\ (Z_0) = (1/2h^3)*\{(d_1^2-d_{-1}^2) - (d_1^4-d_{-1}^4)/4 +$$
$$+ (d_1^6- {}^6_{-1})*7/120 + \text{higher order terms}$$

The values of the even differences d^2, d^4 and d^6 will all be situated at the grid points of the measured B-field, while the odd differences will be in-between the points. By making a program which calculates the successive differences between each grid-point and its neighbours in the measured field-map of the median plane in the magnet, one can thus find the values of the derivatives $B^{(n)}(Z_0)$.

From these derivatives one can, according to (2), get the terms in the Taylor-expansion of the components B_Y and B_Z of the magnetic field given by (1). The B-field can be calculated for any values of Y and Z but for the purpose of ray-tracing it is most convenient to obtain the values for the two-dimensional field-map with a square grid. Because of the loss of significance of the numbers as one goes to higher order differences, only terms up to the fourth difference, d^4, were included in the calculations. Even with this restriction on the Taylor-expansion we found that the differences between the values of the measured field were too small, so that higher order derivatives fluctuated in an un-physical way. To get rid of this problem we chose to use only every fifth measured value in the median-plane, and got a grid mesh of 10 mm in the resulting field-map. These calculated values out of the median-plane of the magnet was compared with the results obtained with the program MAGNET, and it was found that they agreed to better than 1% for both the B_Y- and B_Z-component of the magnetic field.